Dual Species Er-K experiment for the study of impurities in a dipolar quantum gas

University of Oxford, Department of Physics, ALP

Jiri Kucera, MSci

27 August 2021

Abstract

In this report, I describe the current state of the Oxford dual-species dipolar quantum gas experiment and my contribution to its completion during the first year of my DPhil studies. At the moment, production of large number (up to 10^8) of ultracold Erbium (Er) atoms is achieved by transverse cooling and Zeeman slowing via the 401 nm transition and by implementation of a Magneto-Optical Trap (MOT) that addresses the (narrow) 583 nm transition. Additional optical and vacuum systems are currently being built that will introduce cold Potassium (K) atoms into the dipolar Er bath. Both of these systems are discussed in detail. Specifically, the design and assembly process of the 2D+ MOT chamber for the K atoms is described and the mechanism as well as our specific realization of ^{39}K / ^{41}K cooling via the D1 and D2 lines is reported. In our setup and after the initial MOT stages, both the Er and K atoms will be sequentially loaded into a 1030nm crossed beam optical dipole trap (ODT), force-evaporated to quantum degeneracy and optically transported to a glass science cell for further experimentation. A simulation was created to optimize the evaporation process. We briefly describe the theory of dipole trapping, the specific geometry of our system and the thermodynamical model implemented in the simulation and present the reader with preliminary results. Furthermore, the physical relevance of dual species experiments is discussed in relation to dipole-dipole interactions, polarons and more broadly impurity physics. Lastly, an attempt is made to present current state of the art in experimental dipolar cold atom physics and next steps are outlined that need to be taken in order to achieve our experimental goals.

Declaration

I declare that this work has been composed solely by myself and that it has not been submitted, in whole or in part, in any previous application for a degree. Except where states otherwise by reference or acknowledgment, the work presented is entirely my own.

Acknowledgements

I would like to thank my colleagues and labmates - Milan, Lucas and Peter - and my supervisor Rob for all the help and guidance they have provided me with during the past year. I can imagine it was not easy to put up with the barrage of questions I directed their way, especially given my lack of previous experience with experimental physics. I really appreciate their patience and trust.

I also need to mention my housemates (one in particular) who managed to keep me sane during the several lockdowns that we experienced together. This applies to my fellow runners and volleyballers too!

Lastly, big thanks goes to Mark Ijspeert for helping me tremendously with glue desiccation and curing and to Matteo Sbroscia for enlightening and helpful discussions.

Contents

Chapter 1

Introduction

Generation of coherent, narrow frequency light in the form of laser [1] opened up many doors in the field of atomic physics. It allowed for an unprecedented level of control and manipulation via addressing the internal quantum states of atoms. Subsequent developments in laser cooling and trapping techniques [2] lead to the first experimental realisations of a degenerate bosonic gases in 1995 using rubidium (Rb) and sodium (Na) [3, 4]. The first fermionic species followed shortly thereafter [5] and the repertoire of "coolable" atoms has been growing rapidly ever since. Up to this date, 13 atomic species (see figure 1.1) have been cooled to quantum degeneracy using a variety of techniques that, in one way or another, bypass the Doppler limit [6, 7, 8, 9]. Moreover, considerable amount of work is currently being put into laser cooling of molecules [10, 11, 12, 13].

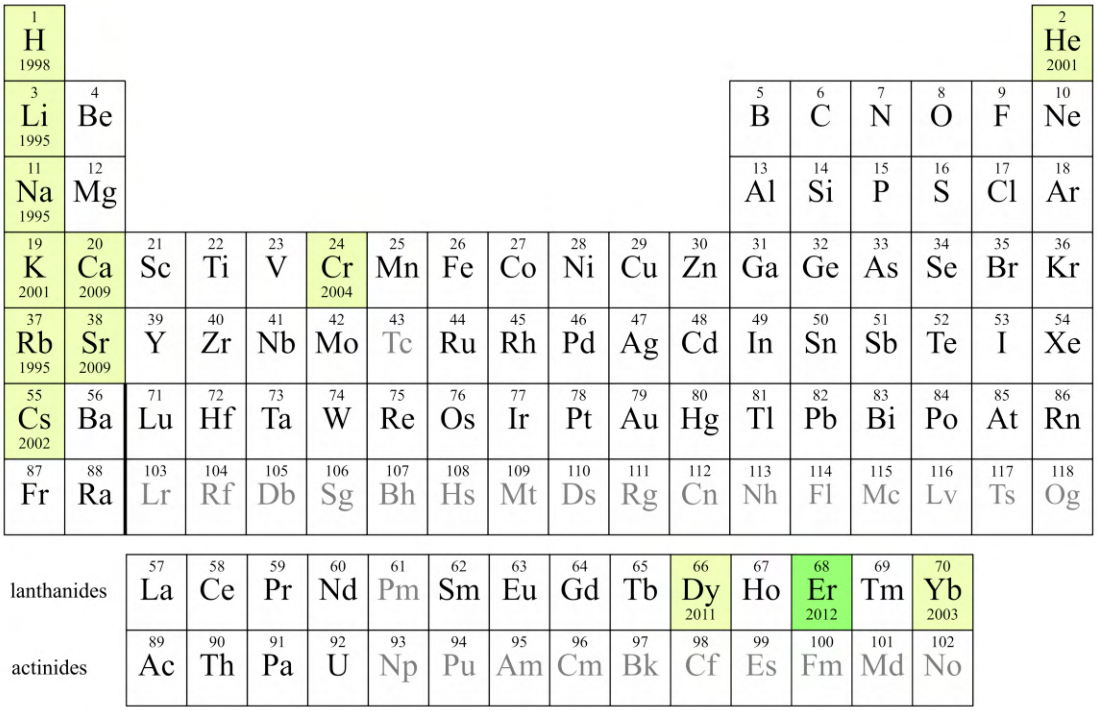

Figure 1.1 – Periodic table with all the elements that have been cooled to quantum degeneracy highlighted in yellow and Erbium shown in green. Potassium is located in group 1 amongst other alkali metals. The number below an element denotes the year when this feat was first achieved. Figure taken from [14]

With its high degree of tunability, cold atoms are a perfect candidate for quantum simulations [15]. The extent of laser light manipulation that is now possible [16, 17] together with a suitable combination of electric and magnetic fields allows one to create almost arbitrary potentials. One can, therefore, mimic and control many-body systems that are experimentally difficult to access. A prime example of this are optical lattices created by interference of a number of laser beams. Resulting potentials possess translational symmetry and allow one to directly probe phenomena that otherwise occur in solids, bridging the gap between condensed matter and ultracold gases. Optical lattices have been used to investigate the Mott insulator to Superfluid phase transition [18], observe exotic states of matter such as Anderson localization or Bose glasses [19, 20] and to shed some light into topological phases of matter [21, 22] - to name a few applications.

Thanks to the relative ease with which one can engineer exotic Hamiltonias, quantum gases can also be used to realise theoretical concepts and test their validity. For example, a novel box potential was used to create a homogeneous BEC [23] which, in return, offered insight into weak collapse and turbulence in a quantum gas [24, 25]. Other examples include the investigation of superfluid vortices [26, 27], dynamics of phase transitions [28, 29], BEC-BCS crossover [30] or the effects of lower dimensionality [31, 32]. Some attempts have also been made that step outside the boundary of the microscopic world and try to simulate cosmological high-energy effects such as Hawking radiation [33] or the Unruh effect [34].

Low energies, long lifetimes and high sensitivity to external perturbations have also made cold atom experiments suitable for more applied purposes. Cold atomic clocks are widely used as a standard of timekeeping [35, 36] and the recent miniaturization efforts have brought them ever so closer to everyday use [37, 38]. Devices based on cold atoms are also used for gravimetry [39, 40] with recent proposals pointing to them as potential candidates for gravitational wave detectors [41, 42].

So far we have omitted the discussion of atom-atom interactions. Vast majority of the experimental endeavours described above involved neutral, alkali atoms. These interact via short range Van der Waals forces which can be well approximated by a contact hard-sphere-like interaction. Such interaction is then completely described by a single parameter - the scattering length - which is, at low temperatures, independent of the energy of colliding atoms [43]. The magnitude of the scattering length affects many properties of quantum gases ranging from their spatial extent to the rate of rethermalization (or their collective correlated behaviour). It is, therefore, of great interest to the experimentalists and theorists alike. The discovery of the so called Feshbach resonances [44, 45] was a major breakthrough in cold atomic physics because it allows one to tune the scattering length using an external magnetic field. Using this technique, the interactions can be made repulsive, attractive or completely disabled. Feshbach resonances can even be used to reach the *unitary regime* where the scattering length diverges and the quantum gas possesses universal properties [46, 47].

Contact interactions provide rich yet somewhat limited landscape for exploring quantum phenomena at the microscopic scale. Lately, a new type of interaction made its appearance in the already powerful toolkit of cold atom experiments. The dipole-dipole interaction (DDI) is both long-ranged and anisotropic, making the resulting system heavily dependent on trapping geometry and potentially exhibiting novel exotic behaviour [48, 49]. DDI can be realised in two ways - using an electric or

magnetic dipole. In practice, the former is achieved with the use of polar molecules - the alkali being the most prevalent [50, 51, 52] - or highly excited Rydberg atoms [53]. The latter involves using atoms with an intrinsically high magnetic dipole and will be the main focus of this report.

Evolution of laser cooling techniques allowed for the first Bose-Einstein condensation of Chromium [54] - a transition metal with a magnetic moment of $6\mu_B$ - followed by the lanthanides Dysprosium ($10\mu_B$) [55] and Erbium ($7\mu_B$) [56] about 10 years ago. This initial success unlocked the door leading to a plethora of exotic many-body phenomena. For example, the theoretically predicted *roton* minimum [57, 58] in the excitation spectrum of a dipolar Bose gas or liquid Helium was observed [59, 60] which arises from the anisotropic interaction of the dipoles in a confined geometry. Tuning the depth of this roton minimum can result in the collapse of the atomic cloud followed by formation of *quantum droplets* - spatially ordered regions of condensed gas that have a well defined volume and density [61, 62, 63]. Furthermore, careful choice of parameters can lead to formation of droplets that show spatial ordering as well as phase coherence across the system - the so called supersolid phase [64, 65, 66].

Motivated by close correspondence with condensed matter systems, dual-species cold atom experiments have emerged over the last decade in which one species plays the role of an *impurity* whereas the other provides and interacting background. If the two species are fermionic [67, 68], for instance, then the combined system resembles the Kondo problem [69] in which a magnetic impurity is immersed in a sea of electrons. However, if the background species is bosonic [70, 71, 72], the overall situation is similar to an electron moving through a sea of phonons - a picture that is believed to be relevant to understanding colossal magnetoresistance [73] or high T_c superconductivity [74]. In both cases, the impurity creates a disturbance in the background gas which travels with the impurity - a form of an elementary excitation called a *polaron* [75]. These exotic quasiparticles will be the subject of future research in our group.

1.1 Oxford experiment

We now turn the discussion to the experimental setup that is currently being built in Oxford and that is aiming to explore some of the exciting topics described above. Currently, there are several groups around the world that run experiments with dipolar atoms. These include groups in Innsbruck [56], in Stuttgart [62], in Paris [76], in Pisa [77], in Hong Kong [78], at Stanford [55] or at MIT [79] to name a few. We are joining the ranks with our experiment which will produce an ultracold mixture of a bosonic isotope of Erbium and a bosonic isotope of Potassium (for similar setup see [80]). What sets our experiment apart is the use of a novel optical box potential which will effectively create a *quasi two-dimensional homogeneous* trap. A homogeneous system is more reflective of its condensed matter analogues and it avoids unwanted averaging of density-dependent quantities which plagues the more widely used power-law traps. The reduced dimensionality, on the other hand, will allow us to control the DDI across the whole sample by applying an external magnetic field and directly observe roton physics.

It is expected that the rich spectrum of Feshbach resonances of Er and K at relatively low fields will be reflected in their interspecies resonances as well. This,

in combination with other techniques that directly tune the DDI [81, 82], will give us full control over the interactions. With potassium acting as an impurity, we will be able to explore the physics of polarons in a dipolar medium [83, 84] with an unprecedented level of tunability. Such polarons differ from their non-dipolar equivalents in two ways. Firstly, the phonon background that the impurity interacts with has an anisotropic dispersion relation. Secondly, the roton excitations of the dipolar bath will also contribute to the dressing of the impurity in analogy with phonons. RF sepctroscopy [71, 72] in combination with a species selective optical gradient can then be used to measure the lifetime, energy and effective mass of the quasiparticles as a function of impurity-bath and bath-bath interaction strength.

A slightly different yet equally exciting direction can be taken with the experiment in order to investigate ideas related to *quantum computing*. More specifically, the study of open quantum systems could be conducted where the potassium impurity is treated as a *qubit* that interacts with the reservoir in form of the dipolar bath. Usually, it is precisely this coupling to the environment that is responsible for decoherence and loss of information. Recent studies [85, 86] have shown that a special type of reservoir called non-Markovian would allow for backflow of information from the environment back to the system, resulting in restoration of coherence. It was hinted [87] that a quasi-2D BEC of dipolar atoms can be used to realise a non-Markovian reservoir thanks to its roton feature in the excitation spectrum. Coincidentally, similar techniques are required for both the analysis of polarons and manipulation of the potassium quibit such as RF spectroscopy, making these two phenomena suitable for concurrent investigation using our experimental setup.

The rest of the report will go into more detail with regards to the experimental techniques used in our laboratory and the progress that has been made towards building the Er-K double species machine over the last year. The design and building of the potassium addition will be discussed together with several setbacks encountered on the way. The report will also touch on optical dipole trapping and numerical simulation of *evaporative cooling* which is a crucial step towards achieving Bose-Einstein condensation. Lastly, the appendices describe several smaller projects undertaken throughout the year such as construction of a multichannel thermometer or a high precision magnetometer.

Chapter 2

The Erbium experiment

In this section we will describe the atomic properties of Erbium and their relevance to our experiment. The basic theory of laser cooling will be covered followed by a detailed description of its implementation within our setup. An overview of the individual stages of the experiment will be provided as well as a discussion of the latest and future upgrades.

2.1 Atomic properties of erbium

Erbium is a rare-earth element located in the lanthanide section of the periodic table. It is a light, silvery metallic substance that occurs naturally only in combination with other elements and it owes its name to the town of Ytterby, Sweden where it was discovered in 1843. With its atomic number of $Z = 68$ and an average atomic mass of $A = 167.26$ amu it belongs to one of the heaviest elements to have been cooled to quantum degeneracy. Erbium occurs in six stable isotopes (see table 2.1), five of which are bosonic and one fermionic making it suitable for exploring phenomena related to either of the two underlying quantum statistics.

Isotope	^{162}Er	^{164}Er	^{166}Er	^{167}Er	^{168}Er	^{170}Er
Abundance	0.14%	1.61%	33.6%	23.0%	26.8%	15.0%
Statistics	boson	boson	boson	fermion	boson	boson

Table 2.1 – Isotopes of Erbium and their corresponding statistics

Following the noble gas notation, the electronic configuration of erbium is $[Xe]\,6s^2 4f^{12}$ which is a prime example of a *submerged shell* atom with valence electrons filling the outer $6s$ orbital and only partially filling the submerged $4f$ orbital. In the ground state, the two $6s$ electrons are in the $^1S_0$ state whereas the $4f$ electrons are in the $^3H_6$ state. These two states then couple via *jj-coupling* to produce the ground state with $J = 6$, $m_J = 6$ and an overall magnetic moment of $\mu = m_J g_J \mu_B \approx 7\mu_B$. As mentioned before, the magnitude of the magnetic moment is exceptionally high and it enables the study of long-ranged dipole-dipole interactions in many-body ultracold systems.

Complexity of the electronic structure is reflected in the richness of the energy level spectrum as depicted in figure 2.1. Of particular interest are the two transitions at 401nm (blue) and 583nm (yellow) which both provide a route to closed-loop two-level optical pumping without the need for a repump laser. The 401nm transition

is between the ground state and the excited $^1P_1$ state of the $6s$ electrons and has a linewidth of $\Gamma = 30$MHz making it suitable for the initial stages of cooling i.e. Zeeman slowing (see section 2.2). The 583nm transition is between the ground state and the $^3P_1$ state and has a narrow linewidth of $\Gamma = 190$kHz which is instead ideal for Magneto-Optical Trapping due to its low *Doppler Tempereature* of a few microkelvin (see section 2.2).

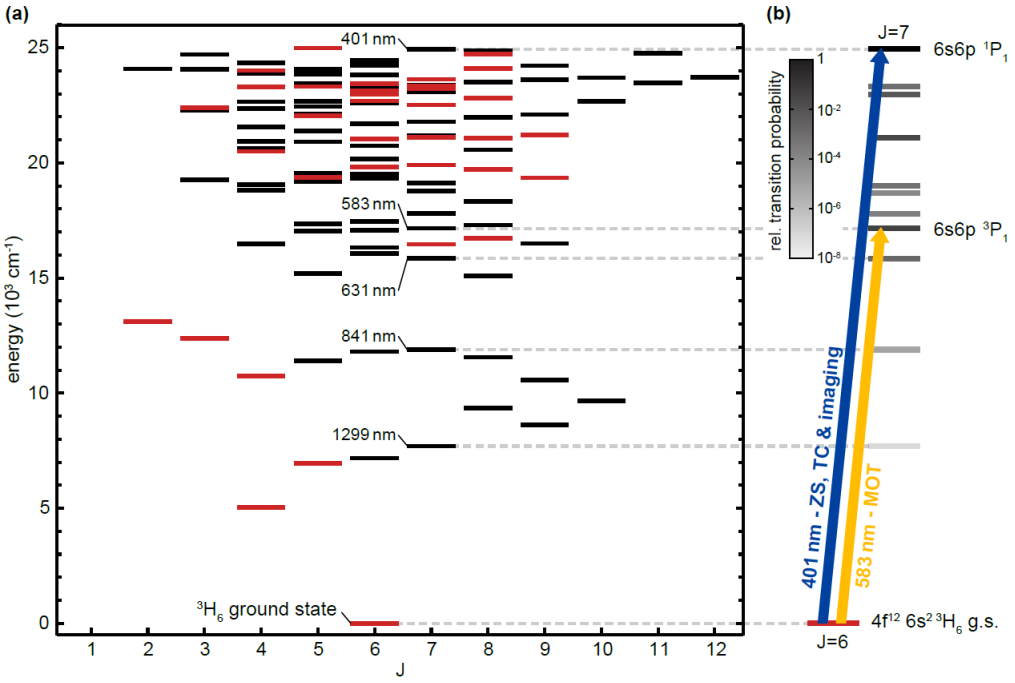

Figure 2.1 – Part of the energy spectrum of Erbium. States with even (odd) parity are shown in red (black). The $J = 6 \rightarrow J = 7$ transitions used for Zeeman slowing and MOT are indicated by the blue and yellow arrow respectively. Figure taken from [88]

2.2 Basics of laser cooling

Electric field interacts with electrons in atoms via a *Hamiltonian* of the form $H = -\boldsymbol{E}(r,t) \cdot \boldsymbol{p}$ where $\boldsymbol{p}$ is the electric dipole and $\boldsymbol{E} = \boldsymbol{E_0} e^{-i\omega t}$ is, in general, a time-varying electric field. In this way, two internal states of an atom with energies E_2 and E_1 can be coupled and a transition between them can be induced by applying an oscillating electric field. The nature of the coupling is encompassed in two parameters - the *Rabi frequency* $\Omega = \frac{1}{\hbar}\langle 1|e\boldsymbol{r} \cdot \boldsymbol{E_0}|2\rangle$ and the *detuning* $\delta = \omega - \omega_0$ where $\omega_0 = \frac{1}{\hbar}(E_2 - E_1)$. In this simple picture, an atom that initially starts in state $|1\rangle$ evolves *coherently* into a *superposition* of the two states and, after some time comparable to Ω^{-1}, comes back to its original state. In the language of *second quantization*, a photon is absorbed from the field only to be re-emitted into the same mode some time later. The picture gets more complicated when one takes into account the fact that a photon can be re-emitted into other available modes. In this case, the atom undergoes an *incoherent spontaneous emission* and decays back to state $|1\rangle$ in a characteristic time Γ. One can then imagine that when the electric (or electromagnetic) field is turned on and $\Omega << \Gamma$, atoms are continuously pumped

into the higher level by absorbing photons and relaxed to the lower level by emitting them, creating an equilibrium population of the two levels.

Laser cooling relies on the fact that, unlike the absorption of a photon from the laser beam which has a well defined direction and hence momentum, the emission is in a random direction and hence on average does not change the overall momentum of the atom. In this way, a laser beam directed against the motion of an atom can slow it down. It can be shown [89] that the scattering force experienced by an atom can be expressed as:

$$F_{scatt} = \hbar k R_{scatt} = \hbar k \frac{\Gamma}{2} \frac{\frac{\Omega^2}{2}}{\delta^2 + \frac{\Omega^2}{2} + \frac{\Gamma^2}{4}} \tag{2.1}$$

where $\hbar k$ is the momentum carried by a single photon and R_{scatt} is the rate of scattering events between an atom and the incoming beam. Note that on resonance, i.e. $\delta = 0$, the magnitutde of the scattering force is maximized.

The detuning δ is a central parameter in all laser cooling experiments. It depends on the frequency of the laser light, making robust frequency stabilization an essential part of any experimental setup (see sections 2.3 and 3.2.2). However, it also depends on the velocity of the atom due to Doppler effect. By deliberately red-detuning ($\omega < \omega_0$) the laser beam, an atom will preferentially absorb photons moving in the opposite direction. This in return ensures that the scattering force is always slowing the atom down. By crossing beams in all the six directions a region in space is created where all atoms experience a viscous friction against their motion - this is the basis of *optical molasses* [90].

Detuning can also be adjusted by directly shifting the internal energy levels which effectively changes ω_0. This is in practice achieved by applying an external magnetic field that introduces a *Zeeman shift* $\Delta E = g_J m_J \mu_B B$ which is different for the two levels involved in the main transition. In this way, one can ensure that an atom stays on resonance and hence experiences the largest scattering force without having to continuously tune the laser frequency - a key idea behind *Zeeman slowing*. In a Zeeman slower, high velocity atoms emerge from a source and propagate along a narrow tube. A laser light which is on resonance with slow atoms is aimed in the opposite direction and a set of coils wrapped along the tube creates a magnetic field profile that ensures that the real detuning is brought close zero at each point along the tube, slowing down the atoms in the shortest possible path and creating a high flux beam of slow atoms. A Zeeman slower is very frequently used as the first stage of atomic cooling and is also implemented in our experimental routine (see figure 2.3).

So far we have only described techniques that "trap" atoms in momentum space via a viscous force. However, in order to increase the atomic density and eventually achieve Bose-Einstein condensation one has to trap atoms in real space as well. A technique that is widely used for that purpose combines the optical molasses with *spatially dependent* magnetic-field-induced energy shifts to create a dense cold atomic cloud - see figure 2.2. It is aptly named *magneto-optical trap* or MOT. The temperature achievable in such setup is termed the *Doppler cooling limit* and is governed by the atom's random walk in momentum space due to photon recoil energy from spontaneous emission. It can be expressed as $T_D = \frac{\hbar\Gamma}{2k_b}$ [91] suggesting that the narrower the transition used for the MOT stage the lower the temperature that can be achieved. In our experiment, a yellow 583 nm transition is used for the

MOT stage with $\Gamma = 190$ kHz. It is also worth mentioning that there exist methods that can achieve sub-Doppler cooling [8, 6].

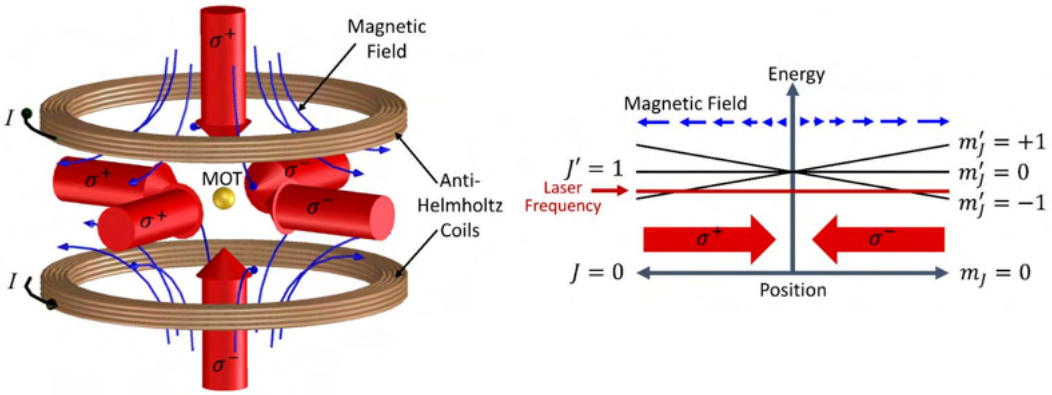

Figure 2.2 – Schematic of a magneto-optic trap. (Left) A MOT is experimentally realised by overlapping an anti-Helmholtz magnetic field with six counterpropagating circularly polarized laser beams that are red-detuned from the main transition. (Right) The inhomogeneous magnetic field induces a spatially-dependent Zeeman shift to the excited state sublevels. Due to the circular polarization only one of the three possible transitions is allowed. Furthermore, as the atom moves away from the center of the trap the sublevel is brought closer to resonance resulting in a position- as well as velocity-dependent trapping force. Figure taken from [92]

2.3 Experimental setup

In this section we will describe the current experimental setup for cooling Erbium and Potassium to quantum degeneracy. Individual cooling stages will be discussed that are already in place as well as planned additions that have been worked on over the past year.

Figure 2.3 shows a top view of the experimental setup. A solid sample of erbium is heated up to 1250°C in an oven. Hot atoms that fly out are collimated using a custom made copper gasket with a circular hole of 8mm diameter. The collimated atomic beam then enters a region where two retroreflected 401nm laser beams slow down the atoms in the two transverse directions, further reducing the spread of velocities and focusing the beam - the so called *transverse cooling* stage.

Afterwards, the atoms enter the Zeeman slower tube (56 cm in length, 8 mm inner diameter) where a counter-propagating 401nm beam in combination with water-cooled coils wrapped around the tube slows the atoms down to $v \approx 100 ms^{-1}$ (see section 2.2). The thin tube also works as a differential pumping segment by maintaining a steady pressure difference between the high vacuum (10^{-7} mbar) part of the experiment on the oven side and the ultra high vacuum (10^{-11} mbar) part on the MOT chamber side.

Finally, the pre-cooled high-flux beam of atoms enters the MOT chamber. Here, six circularly polarized 583 nm laser beams penetrate the chamber from all directions, providing the viscous scattering force to further cool the atoms. Note that only the four beams that are in the horizontal plane are depicted in figure 2.3.

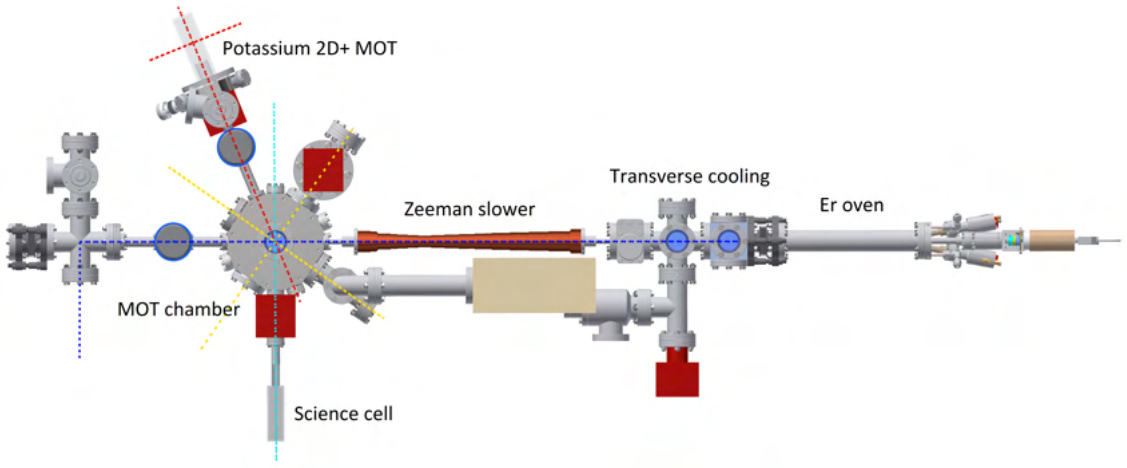

Figure 2.3 – 2D model of the experimental setup. Atoms fly from the oven and are transversally cooled before being slowed in the Zeeman slower. They are then trapped in a MOT in the central chamber and loaded into an ODT (section 4.3). Future plans include optically transporting a BEC of Er/K into a glass science cell and conducting a series of experiments there. A planned Potassium extension is shown in the top left part of the figure. It consists of a glass cell and a vacuum chamber that will host a 2D+ MOT (section 3.1.2) which will serve as a source of cold K atoms. Dashed lines indicate the different lasers beams that are used for the different stages of the experiment. Blue - Zeeman slower; Yellow - Er MOT; Red - K 2D+ MOT; Cyan - ODT. Note that imaging beams, K 3D MOT beams and top ODT beam are not shown for clarity.

Concurrently, a set of coils wrapped around the chamber provides a magnetic field gradient in all directions and hence traps the atoms in the center.

During a 300ms ramp, the MOT is compressed increasing the cooling efficiency at the expense of lowering the capture velocity. The atomic cloud is then loaded into a crossed beam optical dipole trap (see section 4.3) that operates at 1030 nm. At the moment, we can load approximately 10^7 atoms at temperatures of around 50μK. For more technical details of the experimental procedure refer to [14].

So far, we have described what has been achieved in the past. In the following paragraphs we will focus on more recent developments and on work that is currently being done to expand the experiment. A next step towards reaching quantum degeneracy involves evaporative cooling of atoms in the optical dipole trap (ODT). A simulation is under development (see section 4.4) that will be used to optimize this complex process in order to maximize the number of atoms and the final phase space density. To characterize the ODT, it is crucial to know the polarizability of the atoms. This can be measured experimentally [93] but also calculated theoretically from spectroscopic data. The latter approach was adopted in this work (see section 4.2). Furthermore, the profile of the beam needs to be characterized to ascertain the waists of the beam and hence the overall geometry and trap depth. This was done and the data is presented in section 4.3.

After the evaporation stage, we plan to transfer the atoms into an all-glass *science cell* with maximized optical access and commence a series of proposed experiments (see sections 1.1 and 5.2). Some of these experiments involve the addition of Potassium as a second species. For that purpose an extension to the current setup was designed that acts as a source of cold K atoms. This includes a separate glass cell

evacuated to approximately 10^{-7} mbar and connected to the main MOT chamber via a differential pumping section. Within the glass cell, a separate MOT stage is realised solely for the K atoms which slows them along two axes and pushes the atomic cloud into the main MOT chamber along the third axis - the so called *2D+ MOT*. Once the K atoms enter the central chamber they are further cooled via *gray molasses* technique [8, 94] and subsequently evaporated in the same ODT as Erbium atoms. Over the past year, major part of the extension was built including the essential optical systems for addressing the D1 and D2 transition lines as well as most of the vacuum parts. This is discussed in detail in the following chapter.

To serve as a conclusion to this section and also as a testimony of the difficulties one can encounter while doing experimental science, we present a brief account of a few issues that we came across during the course of the past year and how they were dealt with. While analysing fluorescence data from the MOT it was observed that the position of the center of the cloud is unstable - see figure 2.4 left. Initially, it was suspected that a stray magnetic field - possibly a result of an induced magnetization in one of the metal parts - was responsible. For that purpose, a high sensitivity magnetometer was built (see A.1) and placed directly above the chamber. However, no magnetization hysteresis effects were observed. Later it was discovered that some of the mirrors used to steer the MOT beams into the chamber were faulty and produced non-uniform polarisation across the beam which resulted in some of the reported cloud jitter. The rest of the defect was due to an instability in the yellow laser frequency. Originally, a hollow cathode lamp (HCL) was used as a reference to lock the laser but due to the narrow linewidth this method proved to be unstable. Furthermore, the HCL stopped working earlier during the year. For those reasons, it was decided that a high finesse cavity will be bought to replace the HCL. The cavity was recently successfully installed but resulted in several months of down-time for the main experiment. At around the same time, it was found out that the Zeeman slower (ZS) was not working optimally - possibly due to misalignment of the blue (401 nm) beam. Since the installation of the cavity, a lot of effort has been put into recovering the MOT and optimizing all the experimental parameters including the ZS - some improvement can already be seen in figure 2.4.

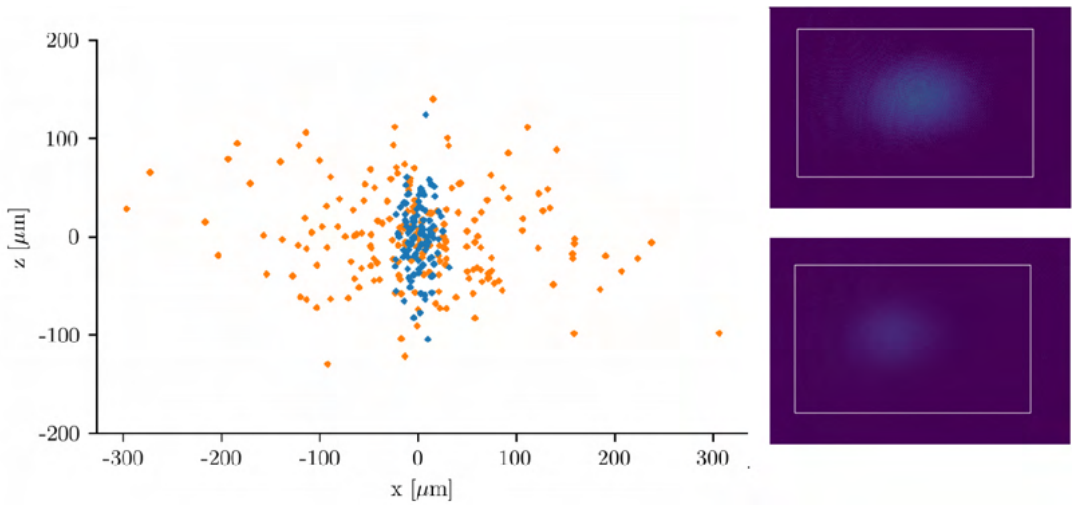

Figure 2.4 – Jitter in MOT position and restoration of MOT. (Left) A plot of the position of the center of the MOT cloud in two directions collected over multiple runs. Orange points indicate readings taken before one of the MOT steering mirrors was replaced whereas blue points indicate readings taken afterwards. Clearly, replacement of the mirror helped the stability in the x direction. It is suspected that similar problem might be plaguing the y direction. This will be investigated further in the upcoming weeks. Figure taken from [14]. (Right) Two images of the MOT cloud. The top image shows the MOT in its current state whereas the bottom is two weeks old. The MOT loading stage is currently being optimized including the alignment and magnetic fields of the ZS stage. Despite the considerable progress, we haven't yet been able to recover the loading numbers achieved at the end of the calendar year prior to the HCL failure.

Chapter 3

Potassium - the second species

In this section we will focus on the addition of potassium (K) to the Erbium experiment. We will discuss the cooling techniques that we are planning to implement in relation to the complex energy level structure of K. The design of the optical systems will be described as well as the current state of the setup. In the last part, a thorough account will be given of the K vacuum extension that is currently under construction.

3.1 How to cool potassium?

3.1.1 Atomic properties of potassium

Potassium is a pale silvery soft metal with atomic number $Z = 19$ and average atomic mass $A = 39.10$ amu that belongs to the group of Alkali metals. It has three stable isotopes, two of which are bosonic and one fermionic (see table 3.1). In our experiment, we focus on the bosonic isotopes ^{39}K and ^{41}K with bigger emphasis on the latter due to its favourable scattering properties.

Isotope	^{39}K	^{40}K	^{41}K
Abundance	93.26%	0.01%	6.73%
Statistics	boson	fermion	boson

Table 3.1 – Isotopes of Potassium and their corresponding statistics

The electronic configuration of potassium $[Ar]\,4s^1$ is deceptively simple with only one hydrogen-like valence electron (as is the case for all the alkali metals). However, its poorly resolved hyperfine structure makes it difficult to cool using conventional techniques. Despite this, our choice of it as the second species is justified by several factors. Firstly, it has both bosonic and fermionic isotopes readily available. Secondly, the transitions used for cooling (see figure 3.1) are addressable by widely accessible lasers. Lastly, the existence of Feshbach resonances at moderate fields gives access to various interaction regimes. Furthermore, the cold atom community, including several members of our research group, has extensive experience with successfully cooling K to quantum degeneracy [95, 96].

Current state of the art experiments use a two-transition scheme for cooling ^{39}K and ^{41}K (see figure 3.1). The D2 transition at 767 nm ($^2S_{1/2}$ to $^2P_{3/2}$) is used for initial 2D+ MOT cooling stage (see section 3.1.2) as well as later compressed MOT

(cMOT) stage. The D1 transition at 770 nm ($^2S_{1/2}$ to $^2P_{1/2}$), on the other hand, is used for the cMOT and gray molasses to reach sub-Doppler temperatures. Tight hyperfine structure allows for radiative decay into dark states resulting in a need for *repump lasers* for both transitions. In the following section we will outline the conceptual ideas behind the different cooling stages.

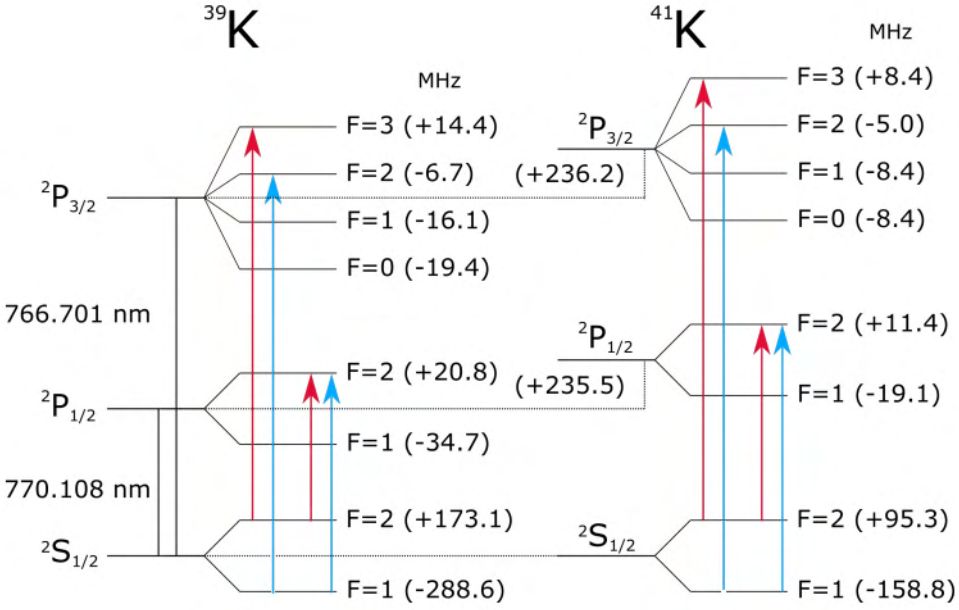

Figure 3.1 – Energy levels of the two bosonic Potassium isotopes and the corresponding transitions used for cooling. The $^2S_{1/2}$ to $^2P_{1/2}$ transition is the so called D1 line whereas the $^2S_{1/2}$ to $^2P_{3/2}$ transition is the D2 line. A repump laser is needed for both lines because, thanks to the tight hyperfine structure, a transition to a different hyperfine state can accidentally occur which allows decay to a dark state at $F = 1$. The purpose of the repump lasers is to depopulate this dark state. Figure taken from [97]

3.1.2 2D+ MOT

Due to limited space on the experimental table a Zeeman slower can't be used as the first stage of cooling. Moreover, the capture velocity of a conventional MOT is too low to be compatible with a high temperature atomic source such as the oven used in the Er experiment. Fortunately, K has a relatively high vapour pressure ($\approx 10^{-7}$ mbar) at temperatures slightly above the room temperature (50K - 80K) making it possible to load a MOT directly from a background vapour. At the same time, high vapour pressure prevents the use of such procedure in the main MOT chamber where UHV ($\approx 10^{-11}$ mbar) needs to be maintained to minimize scattering with background gas and hence maximize the lifetime of a trapped atomic cloud.

Based on these considerations, we decided to implement a pre-cooling stage that consists of a two-dimensional MOT connected to the main MOT chamber via a differential pumping tube. A schematic of the 2D+ MOT is depicted in figure 3.2. The apparatus consists of an evacuated glass cell connected to a slightly heated source of K (not shown in the figure). The cell itself is placed in an oven to maintain an elevated temperature and surrounded by two pairs of coils that create a magnetic

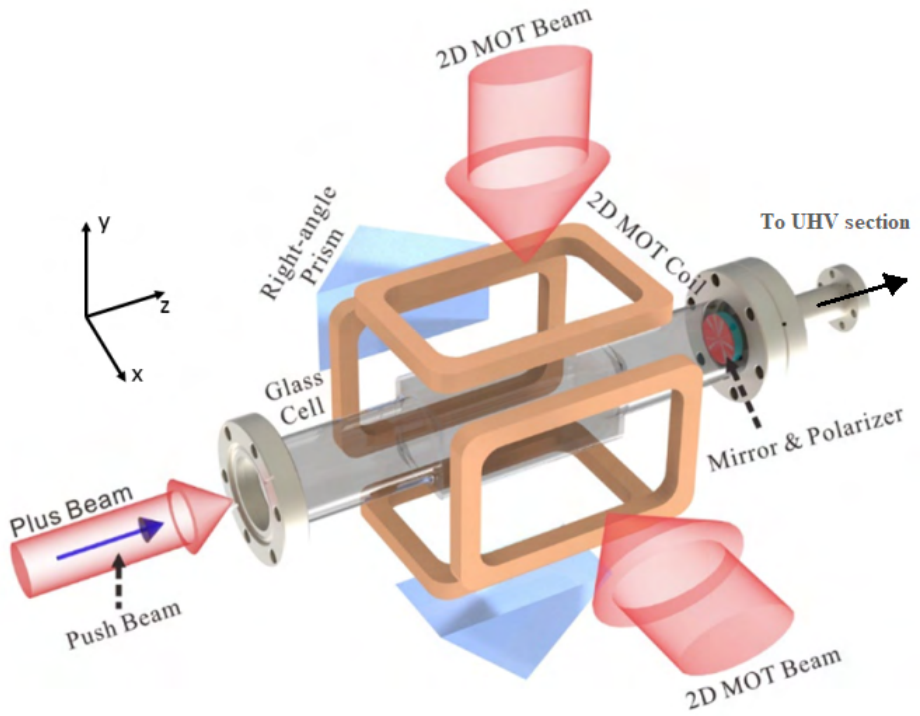

Figure 3.2 – Schematic of a 2D+ MOT. A magneto-optical trapping potential is established in the x-y plane in a similar way to a conventional MOT (see section 2.2) creating an elongated cloud of K atoms in an evacuated glass cell. Another beam is directed along the z direction and retroreflected from a mirror/polarizer tandem situated at the end of the glass cell. This beam provides extra cooling along this direction but no trapping. The mirror/polarizer have a hole in them that leads to a thin differential pumping tube. The lack of confinement creates a flux of atoms in the z direction that passes through the hole and into the main MOT chamber. An additional blue-detuned beam can be used to actively push the atoms through the hole to increase the atomic flux. Figure taken from [96]. Note that in our experiment fur separate beams will be used instead of two retroreflected for the x-y trapping and cooling.

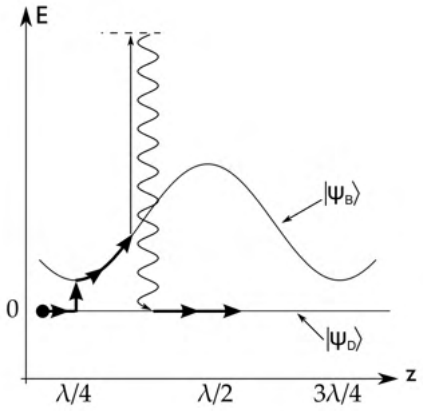

Figure 3.3 – Mechanism of grey molasses. Bright states move in the optical potential (see section 4.2) created by two counterpropagating circularly polarized beams. When they climb up the potential peaks they lose kinetic energy. At the same time, the atoms can get excited into a third state at higher energy and then decay into the dark state that does not experience any optical potential. In this way, some of their kinetic energy is lost and converted into a photon and cooling is achieved. Atoms in a dark state can transition to a bright state via collisions and thus re-enter the cooling cycle. This preferentially happens in the potential valleys. Figure taken from [100]

field gradient along the two perpendicular directions (x and y in the figure). Two pairs of counter propagating beams provide a frictional force in the plane perpendicular to the axis of the cell. In this way an elongated cloud of cold K atoms is created. A third laser beam is directed along the axis and reflected from a linear polarizer/mirror tandem situated at one end of the differential pumping tube. This beam provides additional slowing force along the third direction (hence the "+" sign) and the relative power of its reflected component can be controlled thanks to the polarizer. The lack of spatial trapping along the z axis creates a flux of slow atoms directed towards the differential pumping tube and hence the UHV section. A hole drilled through the polarizer/mirror tandem allows the atoms to escape the 2D+ MOT and proceed to the main MOT chamber. Apart from maintaining a steady pressure difference between the two MOT sections, the differential tube also serves as an indirect filter of slow atoms [98]. This is because it only lets through atoms that are collimated and in order for an atom to be sufficiently collimated it must have spent enough time in the 2D MOT region. Naturally, slower atoms spent more time in the active region and so they will be preferentially let through the tube. Additionally, a blue detuned *push beam* can be aimed through the tube to enhance the flux of atoms into the main MOT chamber.

3.1.3 Sub-Doppler cooling

As mentioned in the previous section, atoms leaving the 2D+ MOT are sufficiently cold to be loaded into a conventional MOT (which is later transformed into a cMOT) that operates with both the D1 and the D2 lines. The Doppler temperature of K under such conditions is around $\approx 150\mu K$. However, the poorly resolved hyperfine structure makes this limit hard to achieve. For that reason, a special technique called *gray molasses* [99, 94, 96] will be implemented that will bring the K atoms to sub-Doppler temperatures.

Gray molasses relies on two effects - *Sisyphus cooling* and *Velocity-selective coherent-population transfer* (VSCPT). Sisyphus cooling is a phenomenon that initially baffled physicists who accidentally realised that they were able to cool atoms below the Doppler limit using conventional molasses techniques [101]. Later it was explained [6] that the effect arises from the combination of a periodic light shift potential created by interference of counter-propagating beams and a position-dependent coupling of two ground sates via a third excited state. Sisyphus cooling is widely used to beat the Doppler limit. However, it can't be realised in three level systems with poor definition of levels - for example in potassium. This is where VSCPT enters the picture. It can be shown [102] that in a three level system where one ground state $|F = 1\rangle$ is coupled to an excited state $|F' = 2\rangle$ via a laser of frequency ω_R and the other ground state $|F = 2\rangle$ is coupled to the excited state via frequency ω_C, a special resonance condition $\delta_R - \delta_C = \delta_{Doppler}$, where $\delta_{R/C}$ are the respective detunings of the lasers and $\delta_{Doppler}$ is the Doppler shift of the atom, results in formation of two states which are a coherent mixture of the two ground states. One is called the *bright state* or $|\Psi_B\rangle$ and interacts with the incoming radiation in the usual way. The other is called the *dark state* or $|\Psi_D\rangle$ and it doesn't interact with the radiation. Note that this three level system is analogous to the D1 cooling-repump system depicted in figure 3.1. By making $\delta_R - \delta_C \approx 0$, this process will preferentially happen for slow atoms with $\delta_{Doppler} \approx 0$. We are then left with a picture in which the coldest atoms in a MOT form these dark and bright states. The bright states move in the periodic potential created by the counter-propagating beams. As they climb the peaks they loose kinetic energy and cool down - much like in the case of Sisyphus cooling. They can get excited to the $|F' = 2\rangle$ state and then radiatively decay to the dark state which exists at zero potential because it does not interact with the radiation. In this way energy is lost from the system and atoms accumulate in the low velocity cold dark state. This process is schematically summarized in figure 3.3.

3.2 Optics

3.2.1 Experimental table

In order to apply the cooling techniques described above one has to be able to address the D1 (770 nm) and D2 (767 nm) lines and supply repump beams to maintain a closed optical cycle. We use two separate seed lasers[1] for that purpose, each with their own frequency stabilization via a potassium gas cell. The two beams containing both the cooling and repump frequency components are then combined on a *dichroic mirror* and directed into a *tapered amplifier*[2] (TA) for power amplification. Finally, the single beam is split in a controllable fashion into the 3D MOT branch and the 2D+ MOT branch. All frequency detunings are introduced via *acousto-optic modulators*[3] (AOMs) that can be remotely controlled to independently regulate the power and frequency in the D1/D2 cooling/repump beams. The schematic of the full optical setup is shown in figure 1.1. Note that majority of the AOMs are in a double-pass configuration meaning that the overall frequency shift is twice the

[1] Toptica DL Pro tunable diode laser
[2] Toptica BoosTA Pro
[3] Gooche and Housego AOMO 125 series

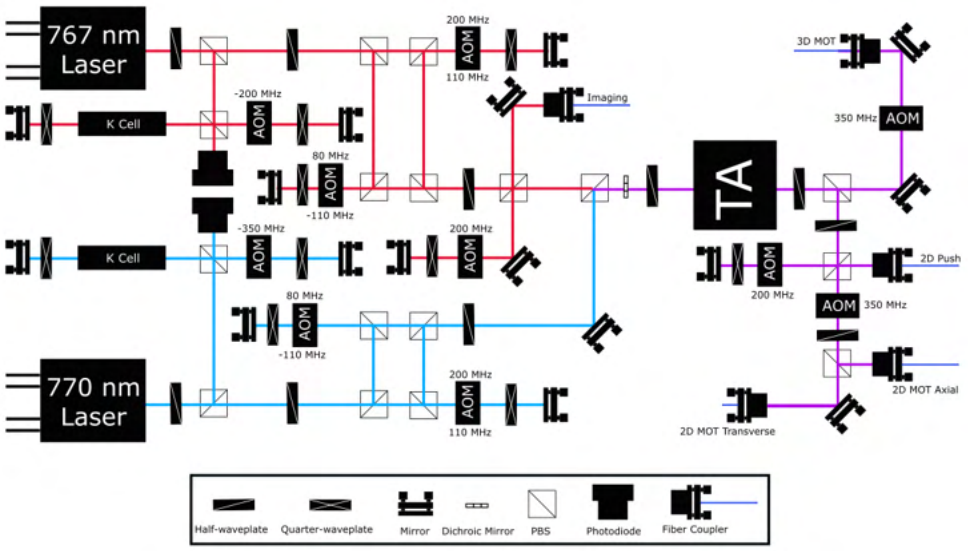

Figure 3.4 – Schematic of the K optical setup

value indicated in the figure. Furthermore, the cooling and repump AOMs have two frequency values ascribed to them - the top refers to ^{41}K and the bottom to ^{39}K. In practice, these are two different AOMs with mirrored beam paths and with only one turned on at a time to address a single isotope. Most of the optics has been built over the course of the last year (see figure 3.5). The alignment of the AOMs has been optimized to reach double-pass efficiencies $\nu > 60\%$ which is particularly crucial for the pre-TA phase since the seed lasers can only output powers close to 60 mW and the TA requires a minimal input of ≈ 12 mW for proper operation. Both of the lasers have been successfully locked using a spectroscopy signal from the K cells (see section 3.2.2. The TA is currently being tested but initial measurements indicate that an input of 21 mW from the pre-TA section produces an output of 2.5W which is sufficient for the intended cooling procedures. In the future, we are planning to install controllable waveplates and implement *machine-learning methods* in order to optimize the cooling sequence by suitably balancing the power ratios in all of the branches.

Most recent work done on the optical setup was focused on beam profiling. Earlier in the year, we realised that the beams coming straight out of the seed lasers could not be successfully collimated using a simple telescope. A series of measurements was conducted in which a snapshot of the beam's cross section was taken at regular intervals and fitted to a Gaussian shape - see figure 3.6. This revealed that both the D1 and D2 seed lasers were divergent in one of the axes. For that reason a series of cylindrical lenses was installed close the aperture of each laser and the beams were successfully collimated.

3.2.2 Laser locking

For stabilizing the frequency of the seed lasers we use a potassium vapour cell as a reference and conduct *saturated absorption spectroscopy* [89] (SAS) to generate a locking signal. In general, absorption features of an atomic gas don't retain their characteristic linewidth Γ due to various broadening effects. Perhaps the most pro-

Figure 3.5 – A photo of the K optical setup. At the beginning of the year only a handful of waveplates and AOMs were on the optical table in addition to the lasers and TA (blue boxes).

nounced one is *Doppler broadening* caused by the thermal distribution of atomic velocities in the gas sample. Atoms from different velocity groups experience different frequency shifts of the incoming beam. The Doppler shift $\delta_D = ku$ for a typical atomic velocity $u \approx \sqrt{\frac{k_b T}{m}}$ at room temperature is much bigger than Γ, making lasers locked to such absorption feature too unstable. SAS gets around this problem by using two counter-propagating beams - one with high intensity called the pump and one with low intensity called the probe. High intensity of the pump guarantees that the excited level population reaches saturation so that any extra light addressing the same atoms as the pump beam will not get absorbed. When the pump beam is scanned through frequency it burns a "hole" in the atomic population at the particular velocity that corresponds to the resonance condition $\delta_{laser} + \delta_{Doppler} = 0$. If the probe is incident on the atomic cloud from the opposite direction it addresses atoms with velocities equal and opposite to the atoms addressed by the pump beam. Consequently, due to its low power most of the probe beam is absorbed and the signal is weak. The situation is very different when the pump beam approaches the center of the broadened absorption feature i.e. when it addresses atoms with velocities close to zero. In this case the probe beam addresses the same atoms and due to the saturation caused by the pump the probe just passes through the sample - we get a strong signal. The width of this signal is comparable to Γ and can be used to lock the laser frequency. This mechanism as at the heart of Doppler-free spectroscopy and is summarized in figure 3.7. We have successfully performed SAS for both the D1 and D2 seed lasers (see figure 3.8). The locking signal is produced by fast modulation of the laser frequency and essentially equates to the derivative of the probe photodiode signal (red). The locking electronics and interface is part

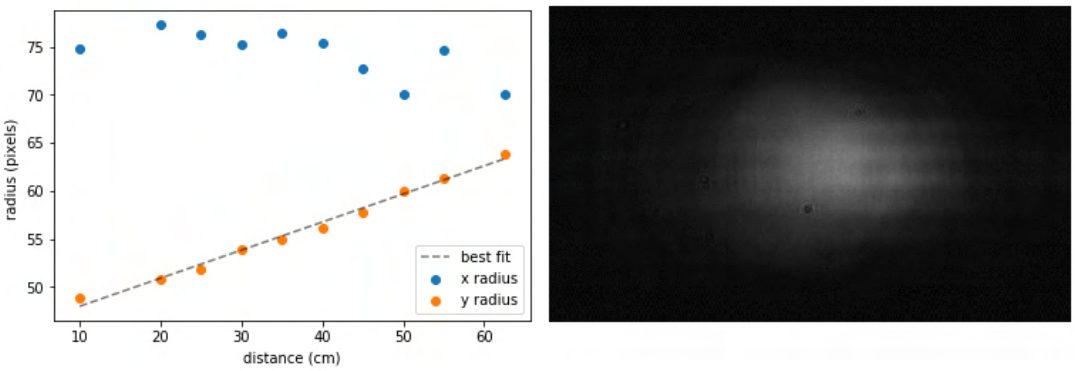

Figure 3.6 – Beam profiling data. (Left) Measured beam waists obtained from fitting a 2D Gaussian to the beam's cross section at several points along the beam. The waist in the y direction shows a diverging trend. For that reason, cylindrical lens was installed at the output of the seed laser to collimate the beam. (Right) Sample of the beam's cross section taken during profiling.

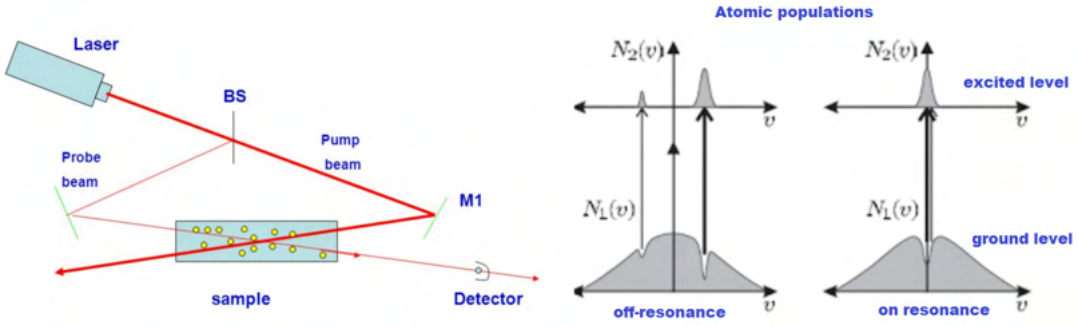

Figure 3.7 – Saturated absorption spectroscopy. (Left) Schematic of a typical experimental setup for SAS. A strong pump burns a "hole" in the sample. A weak probe passes through in the opposite direction and is detected by a photodiode. (Right) Atomic population off-resonance and on-resonance. When off-resonance the two beams address different atoms and the probe gets absorbed whereas on-resonance the pump saturates the sample, the probe passes through and gets detected by the photodiode. The shape of this signal in frequency space is comparable to Γ.

of the hardware and software supplied by Toptica, our supplier.

3.3 Vacuum

3.3.1 Design

The planned potassium vacuum extension consists of several parts. Central to the system is a stainless steel custom vacuum chamber. This has two CF40 flanges that connect to a getter pump[4] and an angle valve for external turbo pump connection. Another flange connects to a bellow that is going to contain the K sample (see below). Through the center of the chamber runs a differential pumping tube with a hole of 2 mm diameter. At the end of the tube is a mounted polarizer/mirror tandem with a drilled hole in the middle to allow atoms to pass from the 2D+

[4]SAES

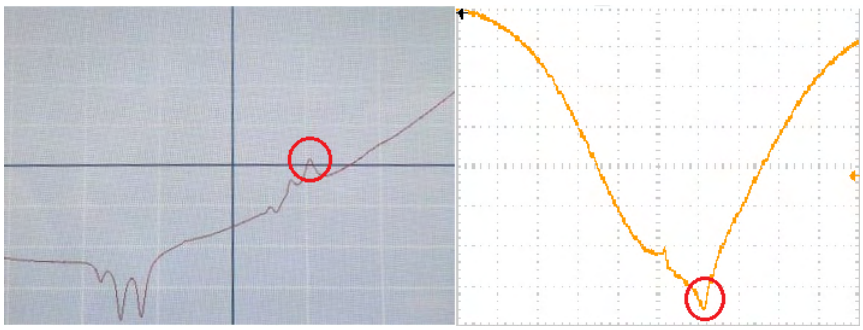

Figure 3.8 – Potassium spectroscopy signals. (Left) D1 line signal (Right) D2 line signal. Red circles denote the lock points. Both lasers were successfully locked using the Toptica PID interface.

MOT region through the differential pumping tube (see section 3.1.2). The custom vacuum chamber has a large flat circular surface with a groove for an indium wire. An AR coated glass cell with a circular glass flange will press against the wire to create a vacuum seal. Use of indium as a sealing agent is justified by the fact that K is highly reactive with other metals and might cause vacuum leaks at the glass-to-metal surface. Upon discussion with other groups, we believe this risk is minimized if indium is used instead. A 3D model of the K vacuum extension is depicted in figure 3.9 a.

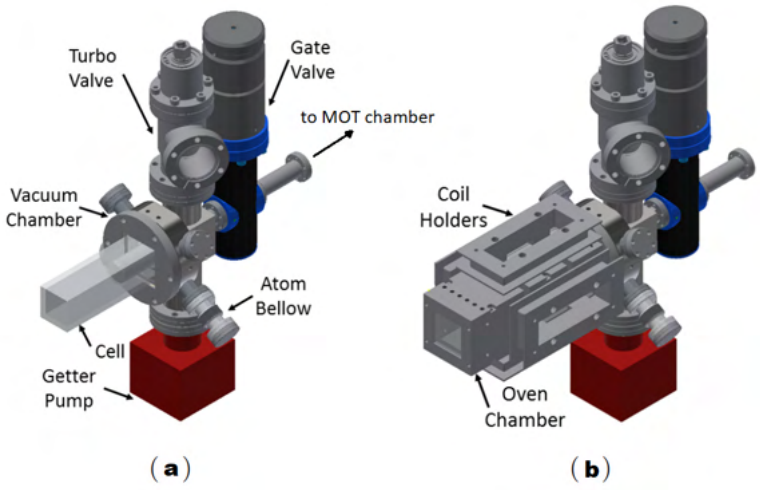

Figure 3.9 – 3D model of the K vacuum extension. Custom vacuum chamber is connected to the main experiment via a gate valve. A getter pump and a turbo pump are also connected to the chamber from the sides together with an atom bellow that will host an ampoule with the K sample. The chamber is sealed off from the front by a glass cell with circular flange. An indium wire will be used to create this glass-to-metal seal. Once the whole system is assembled, a 3D printed oven will be inserted over the cell to keep it warm. The oven will be equipped with AR coated viewports and coil holders for the 2D+ MOT coils. Figure taken from [97].

The glass cell needs to be maintained at a slightly elevated temperature to prevent K atoms from sticking to the sides and reflecting incoming 2D+ MOT beams. For that purpose, an oven was designed that will house the cell without touching its walls. To maintain optical access but also trap hot air inside, the chamber will

have five AR coated viewports. Additionally, a set of four coil mounts is situated on top of the viewports that will hold the two antihelmholtz coil pairs responsible for creating a magnetic field gradient along the two directions perpendicular to the axis of the cell. This is shown in figure 3.9 b.

3.3.2 Assembly

As of now, all the components described above have arrived except for the glass cell and the angled valve used to attach the turbo pump. The final assembly consists of several crucial steps. First, the mirror/polarizer tandem is attached to the differential pumping tube. Second, the chamber is properly cleaned and all the unused flanges are tightly sealed. Third, the glass cell is attached and a seal is created using indium wire. Then, the getter pump, angle valve and bellow containing the K sample are attached and the whole system is connected to the MOT chamber via the gate valve. A turbo pump (connected via angle valve) is used to pump air out of the chamber. Finally, the whole system under high vacuum is gradually heated to temperatures of roughly $\approx 120°C$ and held there for three weeks to release any particles trapped within the walls of the chamber that could potentially cause outgassing and subsequent degradation of vacuum. The oven is an independent external piece and can be added after the bake-out. The first three stages of the assembly have either been completed or attempted over the last few months and will be described in a bit more detail below.

For the mirror/polarizer tandem a fused silica broadband dielectric mirror[5] was used together with a Schott glass linear polarizer[6]. The choice of these parts was mainly influenced by their resistance to elevated temperatures during the bake-out but also by their affordability because the success rate of drilling a hole through their middle was unknown. A supersonic drill with a 1.89 mm head was used for that purpose. On first attempt, the polarizer broke so a new method was devised in which the polarizer was sandwiched between two thicker glass discs and fused with them using resin. Luckily, this method proved successful. There were no major issues with drilling the mirror due to its relatively large thickness. A suggestion was made to attach a glass disc to the reflective side in the same manner as described above in order to prevent chipping of the reflective surface when the drill head enters/leaves the surface. After drilling, both parts were coated with a 100 nm layer of SiO_2 to prevent K from sticking to the surfaces.

Upon consulting with an experimental group in Cambridge, we decided to use an epoxy glue[7] to attach the mirror and polarizer together but also to attach the tandem to the differential tube. The glue that was used required premixing and desiccation in low vacuum to prevent outgassing, followed by a short curing process. Desiccation was done using a turbo pump[8] simply terminated by a flat flange. Initially, a custom 3D-printed cup (see figure 3.10 left) was designed to hold the glue in the pump arm. However, it was observed that the 3D-printed material isn't vacuum-compatible and is causing extensive outgassing. As a replacement, a hand shaped aluminium foil cup was used instead (see figure 3.10 right). The liquid glue sample was left to

[5]BB1-E03, Thorlabs
[6]LPVIS100, Thorlabs
[7]Epotek 920, NASA approved
[8]Asslar D-35614, Pfeiffer

outgas at 10^{-4} mbar for 20 minutes.

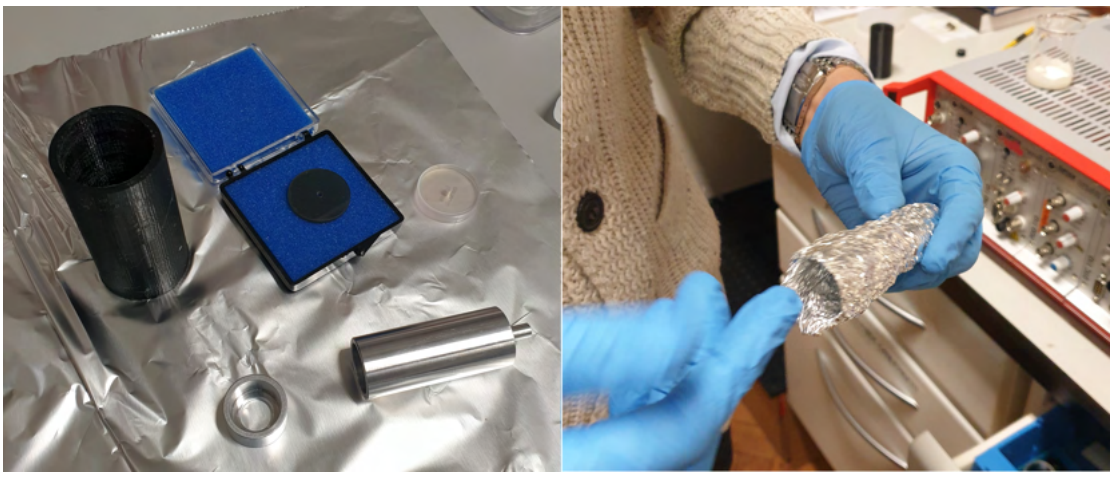

Figure 3.10 – Gluing process - desiccation. (Left) Custom modelled 3D printed cup (black) was planned to hold the glue during desiccation but proved to be incompatible with vacuum. The picture also shows the drilled and coated mirror and polarizer as well as two custom made aluminium pieces that serve as a holder for the K ampoule in the bellow. (Right) Final version of the glue holder made from a hand-shaped piece of aluminium foil.

Prior to gluing, all the relevant parts were left in an acetone ultrasonic bath for 10 minutes. To prevent contact of large flat surfaces and hence air trapping, small cylindrical aluminium spacers (3 mm diameter, 1 mm height) were fabricated and used to separate the tandem and the differential pumping tube (see figure 3.11 left). The glue was applied to one spacer at a time in small quantities using a metal spatula. Alignment of the central hole was achieved by inserting an allen key through all three parts (see figure 3.11 right). The whole chamber was put in an oven and the temperature was slowly (2°C/min) increased to 120°C. The glue was left to cure overnight for 16 hours to emulate the conditions of the bake-out.

Unfortunately, a plastic cover of the glass-to-metal seal surface was left on and the plastic melted into the chamber. We proceeded with removing the plastic using a metal spatula. Special care was taken not to damage any flange surfaces - for those areas a wooden spatula was used instead. Luckily, most of the plastic peeled off readily when handled carefully (see figure 3.12 left). The remaining residues were removed by a combination of mechanical abrasion and chemical agents. We initially used toluene which turned out to make the plastic more fragile when exposed to the solvent for long time and at slightly elevated temperatures. For that reason, we sealed off the vacuum chamber, poured toluene into it and heated it with copper wire (see figure 3.12 right) to approximately 50°C[9] for 2.5 hours. We then proceeded with second round of mechanical removal until majority of the plastic residues were removed. We also tried chloroform but it didn't show any advantages compared to toluene and the lower boiling point made it more volatile.

To test whether the elevated temperatures and exposure to toluene fumes have had any effect on the mirror/polarizer tandem the vacuum chamber was mounted on the optical table and a telescope was used to fully illuminate both components - see figure 3.13 left. A half waveplate mounted on an electronically controllable

[9] a thermocouple was used to monitor the temperature, see appendix A.2

Figure 3.11 – Gluing process - attachment. (Left) First four aluminium spacers were placed at the end of the differential pumping tube. Notice the 2 mm hole in the center that leads to the UHV section. (Right) All components are assembled and aligned using an allen key. In hindsight, the size of the spacers could have been chosen a bit smaller. Also notice the plastic cover sticking out of the aluminum foil in the middle section. This oversight was soon to be regretted.

mount was used to rotate the polarization of the incident light. The reflection off the mirror was collected on a photodiode using lens and plotted as a function of rotation angle of the waveplate. The results are depicted in figure 3.13 right. The measured extinction ratio was 9.9% which is more than sufficient for the purpose of the 2D+ MOT.

After cleaning all relevant parts in acetone bath for 15 minutes and rinsing them with isopropanol, we proceeded with sealing off unused flanges and attaching the glass cell. Indium wire was placed in the groove on the top side of the vacuum chamber with both ends twisted together three times. A metal spatula was used to flatten the twist and make it even with other parts of the wire. Next, the cell was placed on top of the wire and aligned with the chamber. A teflon spacer and steel glass cell holder were pressed against the cell to hold it in place while we began to screw the cell to the chamber. Unfortunately and despite the indium providing very little resistance to the tightening of the screws, the cell cracked during the final turns (see figure 3.14 left). A new cell has been ordered and is expected to be delivered in the upcoming weeks. To test whether the melted plastic didn't leave any residues that could spoil the vacuum, a custom aluminium piece in an approximate shape of the glass cell was fabricated and sealed to the chamber using indium wire (see figure 3.14 right). The chamber was then evacuated using a turbo pump and pressures as low as 10^{-7} mbar were reached suggesting that the plastic didn't have a detrimental effect on the vacuum.

Once the new glass cell and angle valve arrive, the assembly will proceed as planned followed by a three-week bake out. To monitor temperatures of different parts of the K vacuum system during the bake out, a five-channel thermometer was constructed. The technical details are summarized in appendix A.2 including data from controlled heating of the bellow which was conducted to test whether suitable temperatures of the K sample can be reached.

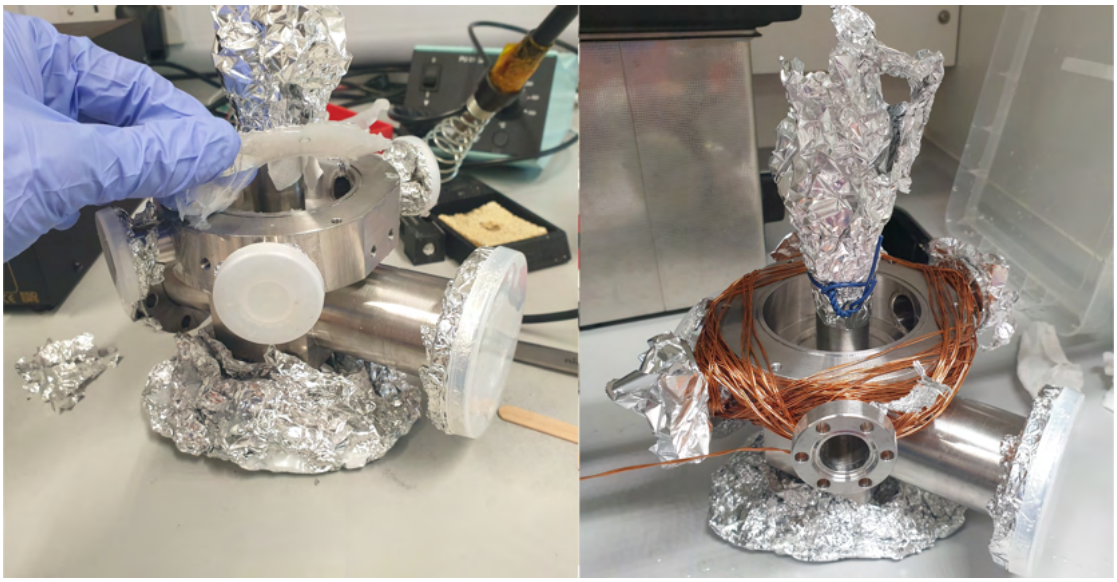

Figure 3.12 – Plastic removal. (Left) Luckily, the plastic that melted into the chamber peeled off readily when appropriate amount of pressure was applied between the plastic layer and the chamber. (Right) To remove the plastic from less accessible areas and also areas that will later be exposed to HV, we heated up the chamber using simple wire and poured toluene into it (not shown). This weakened the plastic enough to remove most of the remaining residues. The optics that had been already successfully attached to the differential tube was covered in a piece of linen and then aluminium foil to reduce interaction with toluene fumes.

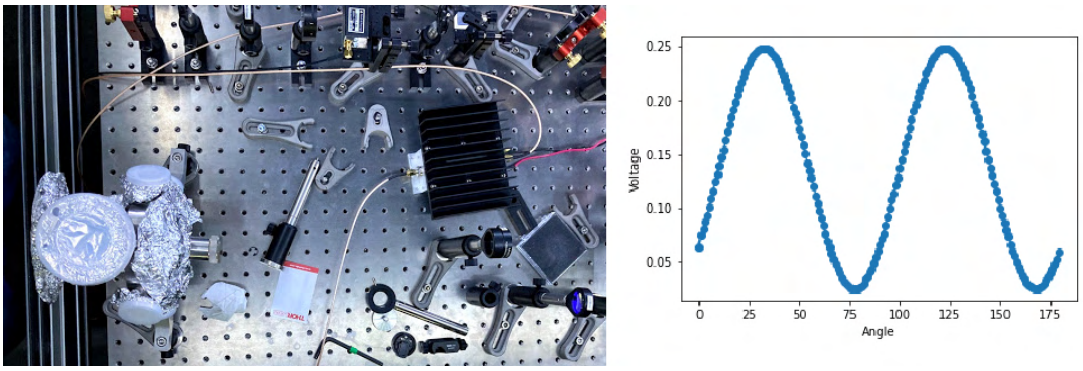

Figure 3.13 – Testing of the 2D+ MOT optics. (Left) Top view of the vacuum chamber mounted on the optical table. An enlarged beam of red (770 nm) laser light was incident on the mirror/polarizer and the reflection was collected on a photodiode. By rotating the polarization we were able to control the ratio of powers in the incoming and outgoing beam. (Right) Plot of data collected by the photodiode. We see a smooth sinusoidal behaviour as expected. From fitting the data to a sine function we could calculate the extinction ratio to be 9.9%.

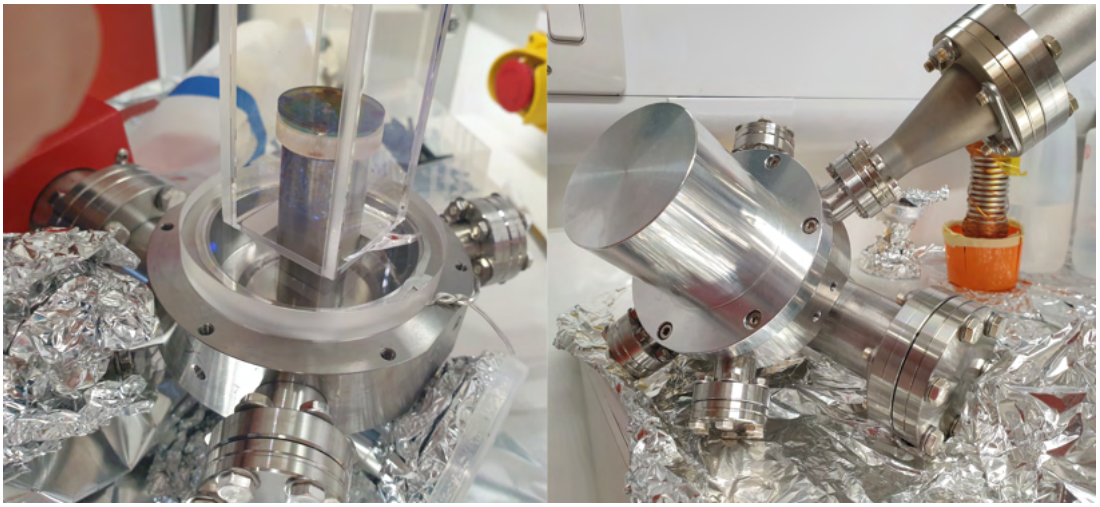

Figure 3.14 – Glass cell breakage. (Left) Fully assembled vacuum chamber with attached glass cell. In the last round of tightening, the cell cracked. It is suspected that the indium wire twisting might be responsible for an uneven pressure distribution which resulted in the crack. We are currently discussing how to deal with this problem. Note that the indium seal is visible through the glass flange as a silvery paste. (Right) An aluminium cap in the shape of the glass cell was used to test the integrity of the chamber and to look for detrimental effects of the plastic on the quality of the vacuum. No deterioration was observed.

Chapter 4

Optical trapping and evaporation

4.1 Optical dipole trap

4.2 The dipole force

In the classical theory of electromagnetism, an electric dipole $\boldsymbol{p}$ placed in an electric field $\boldsymbol{E}(\boldsymbol{r},t)$ experiences a potential $U_{dip} = -\boldsymbol{p}\cdot\boldsymbol{E}$ and an associated force $F_{dip} = -\nabla U_{dip}$. If a neutral atom is placed in an electric field its constituent particles - namely electrons and protons - experience a force in opposite directions. This force shifts the particles in space and hence induces an electric dipole across the atom. Such induced dipole is related to the applied field by a simple relation $\boldsymbol{p} = \alpha\boldsymbol{E}$ where α is the *complex polarizability*. If the field is oscillating such that $\boldsymbol{E}(\boldsymbol{r},t) = \tilde{\boldsymbol{E}}exp(-i\omega t) + c.c.$, one can write the time-averaged potential as:

$$U_{dip} = -\frac{1}{2}\langle \boldsymbol{p}\cdot\boldsymbol{E}\rangle = -\frac{1}{2\epsilon_0 c}Re(\alpha(\omega))I(r) \tag{4.1}$$

here $I = 2\epsilon_0 c|\tilde{\boldsymbol{E}}|^2$ is the intensity of the field, $\alpha(\omega)$ is the frequency-dependent polarizability and the factor of $1/2$ comes from the fact that the interaction is between the field and an induced dipole, not a fixed one. Note that for $Re(\alpha(\omega)) > 0$ the atom is attracted to positions with high intensity $I(r)$. This mechanism is at the heart of dipole trapping.

In a similar way, one can calculate the total power absorbed by the oscillating dipole (and subsequently re-emitted) $P_{abs} = \langle \dot{\boldsymbol{p}}\boldsymbol{E}\rangle$ and hence the photon scattering rate:

$$\Gamma_{scat} = \frac{P_{abs}}{\hbar\omega} = \frac{1}{\hbar\epsilon_0 c}Im(\alpha(\omega))I(r) \tag{4.2}$$

We see that the polarizability $\alpha(\omega)$ is a central quantity that governs the interactions of the atom with the electric field. In order to calculate its value one has to turn to quantum mechanics. Using time-dependent perturbation theory one can show [91] that the energy shift of a certain state $|0\rangle$ under the influence of an oscillating electric field is given by:

$$\Delta E = -\frac{|\tilde{\boldsymbol{E}}|^2}{2}\sum_n \frac{(E_n - E_0)|\langle n|d_i|0\rangle|^2}{(E_n - E_0)^2 - (\hbar\omega)^2} \tag{4.3}$$

where the sum is over all states $n \neq 0$, E_j denotes the energy of the j-th state and d_i is the dipole moment along the direction of the field. From the relation $\Delta E = -\frac{1}{2}\alpha(\omega)\langle \boldsymbol{E}^2 \rangle_t$ the polarizability can be recovered. A more complete treatment takes into account the finite lifetime of the excited states as well as non-spherically-symmetric atoms. A full expression for the dipole potential is then [103, 104]:

$$U_{dip} = -\frac{1}{2\epsilon_0 c} I(\mathbf{r}) \left\{ \mathrm{Re}\left[\alpha_{\mathrm{scal}}(\omega)\right] + \mathcal{A}\cos\theta_k \frac{M_J}{2J} \mathrm{Re}\left[\alpha_{\mathrm{vect}}(\omega)\right] + \frac{3M_J^2 - J(J+1)}{J(2J-1)} \times \frac{3\cos^2\theta_p - 1}{2} \mathrm{Re}\left[\alpha_{\mathrm{tens}}(\omega)\right] \right\} \tag{4.4}$$

here "vect" and "tens" denote the vector and tensor part of the polarizability that arise from the non-sphericality, θ_p is the angle between the field and the z axis, θ_k is the angle between the k vector and z axis, J and M_J denote the total angular momentum and magnetic sublevel quantum numbers of the ground state and $\mathcal{A}$ is the ellipticity of the polarisation. Similar expression can be derived for the photon scattering rate. The expression for the scalar, vector and tensorial components are given in the references [103, 104].

In order to calculate the polarizability as accurately as possible one needs to have a detailed account of the energies and lifetimes of the excited levels. These can be either obtained experimentally or numerically. We use a numerical dataset taken from [93] to calculate the real and imaginary part of the polarizability of Erbium over a range of wavelengths. In the case of our setup, linear polarization at an angle of 90° with respect to the quantization axis of the atoms (z-axis) is used which eliminates the vector term of the polarizability. The plot of the calculated real part of the polarizability is shown in figure 4.1. The optical dipole trap used in our experiment has a wavelength of 1030nm (indicated by vertical line in the figure) for which the real part of the polarizability takes on the value 177.27 a.u.

4.3 ODT setup

In this section we will briefly describe our experimental realisation of an IR optical dipole trap (ODT). The main purpose of the ODT is to load cold atoms ($\approx 10\mu$K) from the MOT and proceed with *forced evaporation* (see section 4.4.1) to cool them to quantum degeneracy. Afterwards, the atoms will be optically transported into the science cell for further experiments. We use a single seed laser[1] with an output power of 45W. The operation wavelength of 1030nm was chosen based on the availability of high power lasers and distance from resonances (see figure 4.1). The outgoing linearly polarized Gaussian beam is split into two using an AOM. This serves as an intensity control between the two beams and also allows to shift the position of one of the beams horizontally by adjusting the driving frequency of the AOM. If the frequency is changed fast enough compared to the typical timescales of atomic motion, the atoms experience a time averaged potential which is equivalent to increasing waist of the beam along that direction - the so called *dithering*. The non-dithered beam is coupled to an optical fibre and guided to the top of the MOT chamber via series of lenses that adjust the final parameters of the beam.

[1] Azurlight systems

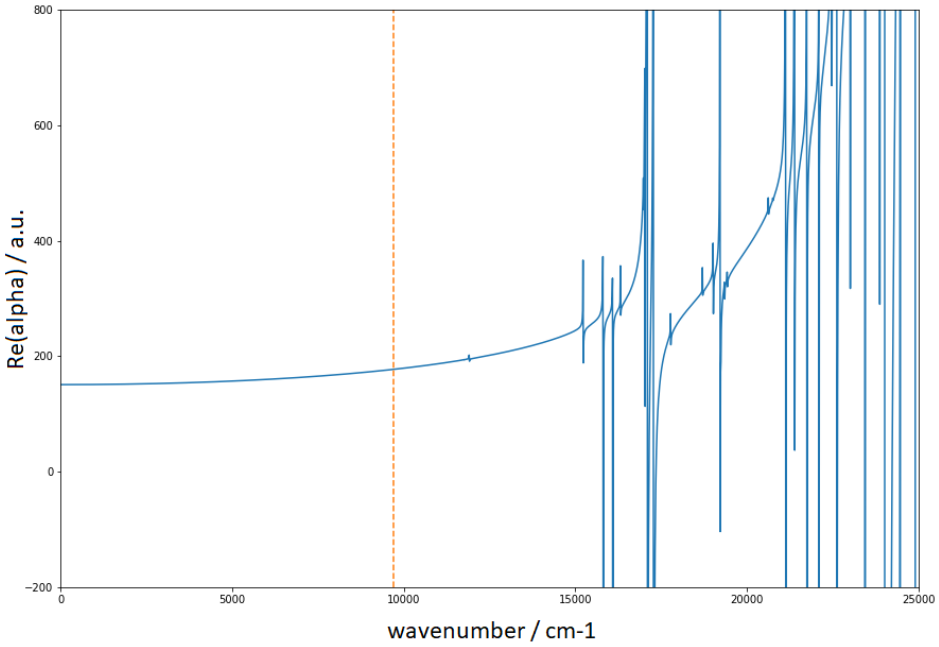

Figure 4.1 – Polarizability of Erbium. Plot of the real part of the poralizability calculated using data from [93]. The sharp spikes indicate a transition at the particular wavenumber where the polarizability is divergent. Note that the spikes in the figure have finite size due to the finite size of the sampling grid in the wavenumber space. Also note that the polarizability in this region is positive resulting in a trapping rather than anti-trapping potential. The operating wavelength of our ODT is shown as the vertical line (orange). The value of the polarizability there is 177.27 a.u.

The dithered beam is directly guided to the MOT chamber via a tandem of tunable lenses which can be electronically adjusted to move the focus of the beam without changing its waists. A schematic of the setup is shown in figure 4.2.

ODT1 penetrates the MOT chamber in the horizontal plane and continues to the science cell (not shown in the figure) where it is terminated by a beam dump. Its polarization is linear and in the horizontal plane. ODT2 enters the chamber in a plane perpendicular to ODT1 and at an angle of 7° to the vertical direction (see figure 4.3 left). Polarization of ODT2 is perpendicular to that of ODT1 and to the vertical direction (quantization axis of the atoms). The foci of the two beams overlap in the center of the chamber to form a crossed-beam optical dipole trap [105]. The power balance between the two beams at the time of loading the trap is $P_{ODT1} = 25$ W and $P_{ODT2} = 5$ W. The purpose of ODT2 here is to create more confinement along the beam of ODT1 by introducing a *dimple* [106] in the center of the trap (see figure 4.3 right, top). This increases the density in the center and hence the scattering rate and evaporation efficiency. Currently, we can load approximately 10^7 atoms at temperatures of around 50μK into the crossed-beam ODT. More work will be done in the future to optimize the loading efficiency with regards to the dithering frequency and amplitude. After the loading stage, power in the beams will be gradually lowered over the course of several seconds and the atoms will be cooled to degeneracy via forced evaporation (see section 4.4.1).

Currently, one of the tunable lenses is removed and the ODT1 beam is being profiled by changing the last lens in the cascade (green circle in figure 4.2). Three different lenses of focal lengths 200mm, 300mm and 400mm have been used and the

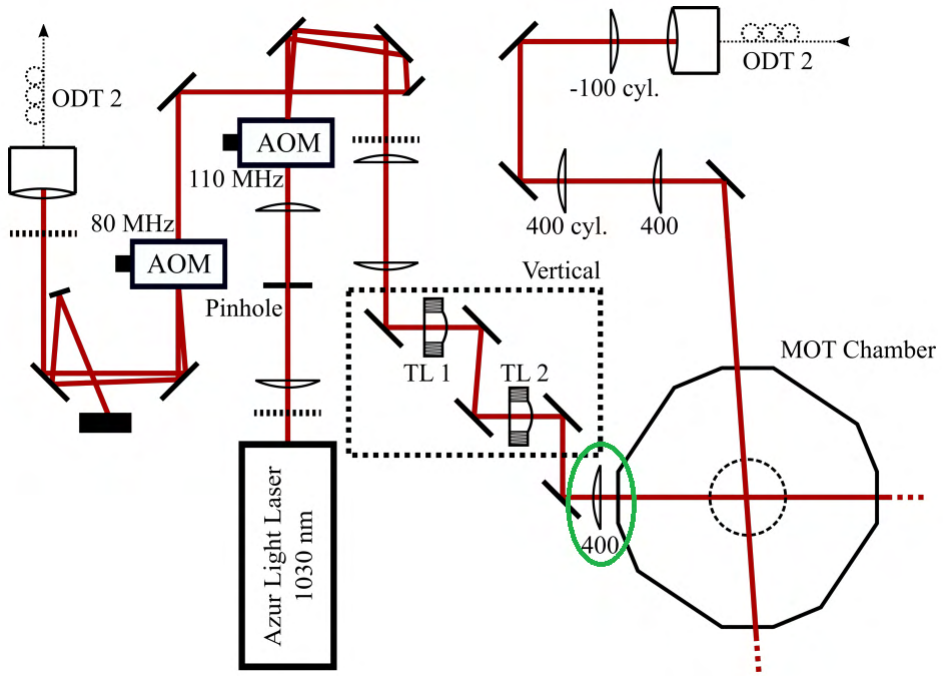

Figure 4.2 – Schematic of the ODT setup. The tunable lenses can adjust the position of the focus of the beam without changing its shape. Since the atoms are attracted to the focus due to the dipole force (see section 4.2 the cloud can be transported along the beam by adjusting the lenses. The last lens in the ODT1 cascade (green) is currently being tested in order to achieve the best confinement. Figure taken from [14].

profile along the beam was measured using a high resolution camera[2]. Simultaneously, the focal power of the tunable lens was adjusted to keep the focus at roughly constant position along the beam. The aim here is to find a lens that provides best confinement along the beam. A snapshot of the beam's cross section was taken at regular intervals around the focus and a 2D Gaussian profile was fitted to the images to obtain the waists of the beam. Additionally, the maximum intensity was measured and the resulting potential depth was calculated (see section 4.4.2). The values were then fitted to a harmonic model to obtain a typical frequency associated with confinement along the beam. The measured data is presented in figure 4.4. While the change from 400mm to 300mm doesn't show much difference, the 200mm lens provides considerably better confinement and will be used for future experimentation. Furthermore, we note that the beam is slightly astigmatic meaning that the foci in the two transverse directions are located at different positions along the beam. A further investigation will be conducted to find the source of this defect and possibly fix it.

[2]CS165MU1 Zelux, Thorlabs

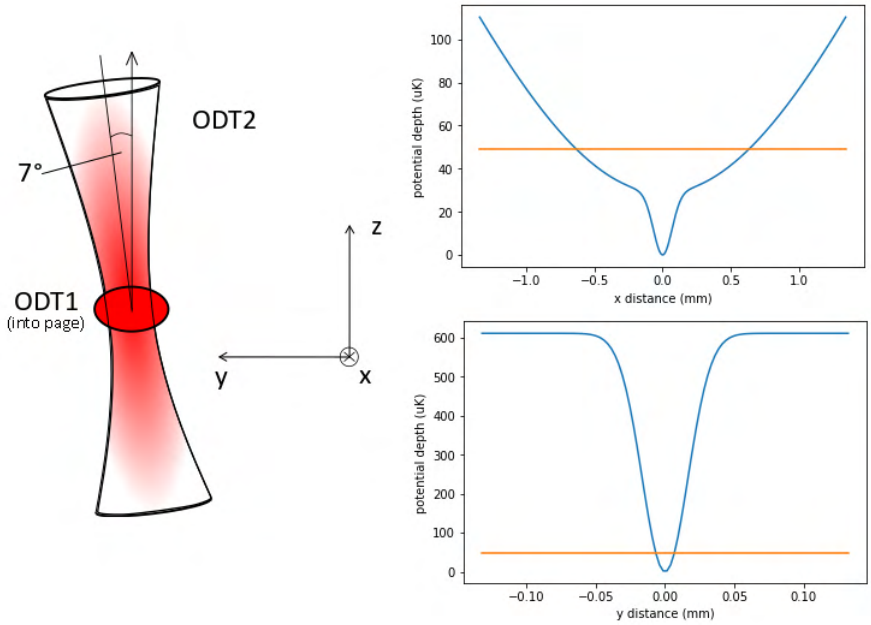

Figure 4.3 – ODT geometry. (Left) ODT1 propagates along the x axis whereas ODT2 comes in at a sharp angle (7°) from the z axis in the z-y plane. The foci of the beams overlap to form a dimple potential. (Right) The potential created by the crossed beams along the x (top) and y (bottom) axis. ODT2 creates a dimple in the potential along the x axis, producing more confinement and increasing the evaporation efficiency. The horizontal line (orange) indicates the typical loading temperature of the atoms.

4.4 Evaporative cooling

4.4.1 The basics

Although sub-Doppler cooling methods can bring the atomic cloud temperature down to several μK, the maximum achievable phase space densities are of the order of $PD \approx 10^{-4}$ whereas the onset of Bose-Einstein condensation happens at $PD \approx 1$ [107]. Fortunately, this seemingly large gap can be bridged with the use of evaporative cooling. The main principle behind this technique is rather simple and mirrors the phenomenon of evaporation we all know from our everyday lives - be it cooling of a coffee mug or our body via perspiration. Atoms confined in a trap collide and thermalize to an equilibrium temperature and velocity distribution. Some of these atoms are fast enough to climb over the potential barrier and escape the trap. If the trap is deep enough, the kinetic energy required to escape it is larger than the average kinetic energy of the atoms in the trap $\bar{E_{kin}} = \frac{3}{2}kT$. That means that when an atom does escape, it carries away more than its share of energy. Consequently, when the remaining atoms rethermalize via collisions their average energy and hence temperature is lower than it was before. In this way, the atomic cloud is cooled down at the expense of loosing atoms (see figure 4.5). There is a catch though. If the trap depth is kept constant, fewer and fewer atoms will have enough energy to escape it because of the cooling effect. At some point, the evaporation will stop and so will the cooling. To counteract this undesirable side effect, one can continuously lower the depth of the trap and thus maintain the efficiency of the evaporation. This

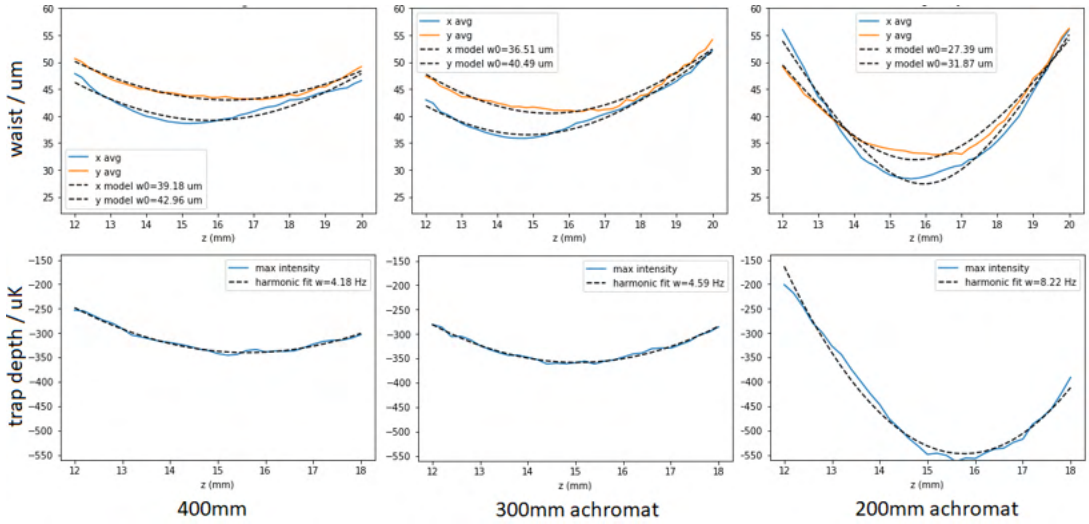

Figure 4.4 – Profiling of the ODT1 beam. Top row shows the fitted waist along the beam in both transversal directions. Bottom row shows the trap depth along the beam as calculated by measuring the highest intensity in a given snapshot. The 200 mm lens shows considerably more confinement and will be used for future experiments.

widely used technique is called *forced evaporation* and will be implemented in our experiment. The main challenge here is to figure out how quickly to lower the trap - too slow and the evaporation will die out; too fast and even the low energy atoms will be able to escape, reducing the cooling effect. Optimization of this process will be discussed in section 4.4.3. There are two main ways in which evaporation is performed. Historically older and currently less prevalent is the radiofrequncy (RF) knife technique [3, 7] in which atoms are placed in a magnetic trap in a low-field-seeking state. An RF field is used to induce transition between this state and a high-field-seeking state that gets expelled from the trap. The frequency of the radiation is tunable and chosen such that it is only resonant with atoms that reach certain depth within the trap. If atoms have enough energy to reach this depth, they are instantly expelled. In this way, the RF field cuts through the trap like a knife and gradually "chops off" more and more of it as the frequency is tuned, lowering the trap depth in the process. The second and more widely used method exploits the dipolar force exerted by a far-detuned high intensity laser beam to trap atoms in an ODT. In this case, the trap depth is simply lowered by reducing the power of the laser beam. There are several differences between the methods. Whilst the magnetic evaporation is heavily state dependent (it needs a low-seeking-state), the optical method is not and allows for trapping of mixtures of states. Furthermore, application of an external magnetic field can beneficially affect the scattering properties of the atoms via Feshbach resonances [109] which is considerably easier to achieve in the case of the optical trap. However, the optical method suffers from the lack of confinement of the atoms along the axis of the beam. Furthermore, as the power of the beam is lowered the shape and typical frequency of the trap changes which is not the case for magnetic trapping where the shape is conserved and only the effective depth is tuned.

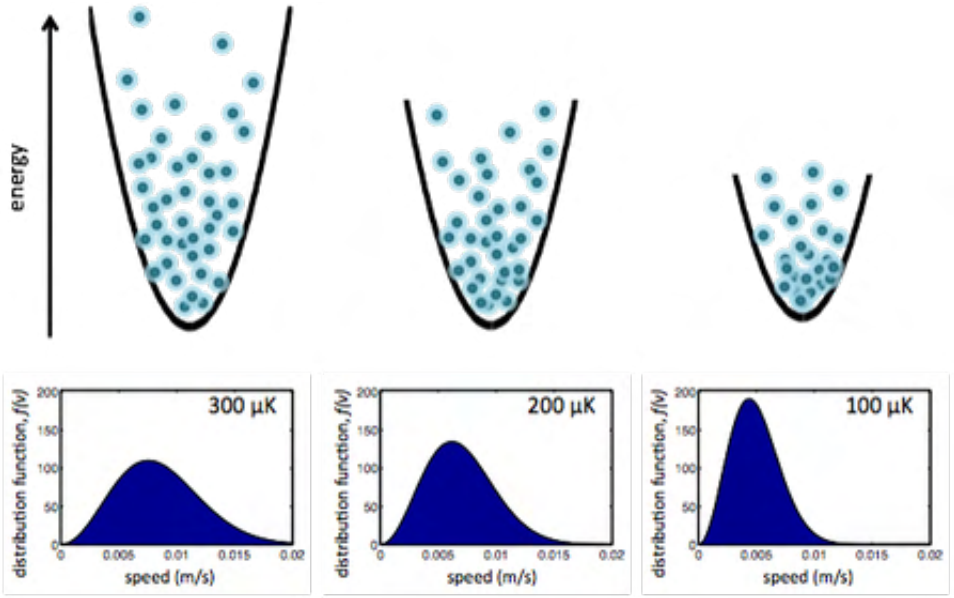

Figure 4.5 – Cartoon of evaporative cooling. As the high energy atoms escape the trap, the remaining atoms reach a new quasi-equilibrium with a lower average velocity and hence temperature. At the same time, the trap depth needs to be lowered to maintain the process at high efficiency. Figure taken from [108].

4.4.2 Optical potential

In this section, we discuss the typical shape and depth of our crossed-beam ODT in order to prepare ourselves for the discussion regarding modelling of atomic evaporation in such trap (section 4.4.3). Using equation 4.1 we can express the potential created by a single Gausssian beam propagating along the x axis as:

$$U_{dip}(\boldsymbol{r}) = -\frac{Re(\alpha)}{\epsilon_0 c}\frac{P}{\pi w_y(x) w_z(x)} exp\left[-2\left(\frac{y^2}{w_y^2(x)} + \frac{z^2}{w_z^2(x)}\right)\right] \tag{4.5}$$

where $w_i = w_{i0}\sqrt{1+(x/z_{Ri})^2}$ is the beam waist at position x along the i-th axis with w_{i0} being the waist at the focus and $z_{Ri} = \frac{\pi w_{i0}^2}{\lambda}$ the corresponding Rayleigh range. The full trap depth can be simply obtained by setting $\boldsymbol{r} = (x, y, z) = (0, 0, 0)$ to yield:

$$U_{trap} = \frac{Re(\alpha)}{\epsilon_0 c}\frac{P}{\pi w_{y0} w_{z0}} \tag{4.6}$$

By Taylor expanding the potential around $\boldsymbol{r} = (0, 0, 0)$ to second order in the coordinates, one can derive an expression for the potential in the form $U_{harm} = \frac{1}{2}m(\omega_x^2 x^2 + \omega_y^2 y^2 + \omega_z^2 z^2) - U_{trap}$ with the trap frequencies given by:

$$\omega_x = \sqrt{\frac{\alpha P \lambda^2 \left(w_{0y}^4 + w_{0z}^4\right)}{m\epsilon_0 c\pi^3 w_{0y}^5 w_{0z}^5}}, \tag{4.7}$$

$$\omega_y = \sqrt{\frac{4\alpha P}{m\epsilon_0 c\pi w_{0z} w_{0y}^3}} \tag{4.8}$$

$$\omega_z = \sqrt{\frac{4\alpha P}{m\epsilon_0 c\pi w_{0y} w_{0z}^3}} \tag{4.9}$$

Figure 4.6 shows a comparison between the full Gaussian expression for the potential and the harmonic approximation plotted along the axis of the beam. A single beam produces a potential that is very close to the harmonic one in the region where the potential is lower than the typical loading temperature of the atoms (green line). However, in the crossed beam setup, the harmonic approximation is only valid within the dimple and fails to account for the "wings" of the potential out of the dimple. This means that the harmonic approximation is only applicable to the case when the temperature is below the depth of the dimple - a crucial observation that will be further discussed in the next section.

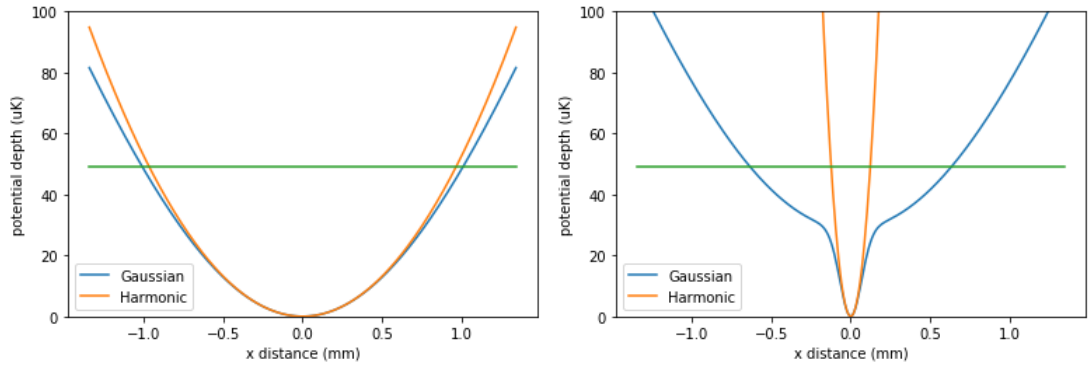

Figure 4.6 – Comparison of the full Gaussian beam potential and the harmonic approximation. (Left) Plot of the potential along the axis of the beam for a single-beam trap. The harmonic approximation is very close to the real potential. (Right) Same plot but for the crossed-beam trap where an additional beam creates a dimple along the first beam. This produces more confinement for the atoms but invalidates the use of the harmonic approximation for temperatures higher than the dimple depth. Horizontal line (green) indicates the typical loading temperature.

4.4.3 Simulating evaporation

As discussed in section 4.4.1, the main challenge of evaporative cooling is to optimize the ramping down of the potential. Generally, the aim is to maximize the final phase-space density (PD) whilst minimizing the particle loss. Moreover, under special circumstances one can also be interested in minimizing the time of the ramp due to some experimental constraints. This can be done directly i.e. by running the experiment with different ramp parameters and looking for the best outcome. However, the functional space of all the possible ramps $U_{trap} = U_{trap}(t)$ is infinite and

even though a limited subset of, for example, exponential ramps could be focused on, the optimum ramp derived in this way is not guaranteed to converge anywhere close to the absolute optimum.

Alternatively, a numerical simulation of the process could be used to explore the functional space more efficiently. There are two fundamentally different ways of approaching the problem. The first and probably more "brute force" approach tries to simulate the dynamics of the particles by calculating the forces acting on them due to the light field and due to collisions with other particles [110, 111, 112]. By keeping track of positions and momenta, the system can be propagated in time in small increments. Such approach does not assume anything a priory about the system and its evolution, making the resulting predictions very robust. However, the simulation is generally computationally demanding. The second approach relies on the language of statistical physics to derive differential equations for the evolution of thermodynamical properties such as temperature or particle number. We outline this method bellow together with our own implementation and present some preliminary results.

We will closely follow the derivations presented in [113] and [114]. The model assumes classical behaviour of the gas, ergodicity of the system and Knudsen regime of the dynamics in which the collisional mean free path is much larger than the size of the cloud. The central quantity that describes the system is the phase-space distribution function $f(\boldsymbol{r}, \boldsymbol{p})$, the evolution of which is determined by the Boltzmann equation:

$$\left(\frac{\mathbf{p}}{m} \cdot \boldsymbol{\nabla}_{\mathbf{r}} - \boldsymbol{\nabla}_{\mathbf{r}} U \cdot \boldsymbol{\nabla}_{\mathbf{p}} + \frac{\partial}{\partial t} \right) f(\mathbf{r}, \mathbf{p}) = T(\mathbf{r}, \mathbf{p}) \tag{4.10}$$

where $T(\mathbf{r}, \mathbf{p})$ is the collisional integral. It can be shown [113] that under the assumption of energy-independent scattering cross section[3] the occupation number $f(\epsilon)$ of trap eigenstates with energy ϵ is given by a *truncated Boltzmann distribution*:

$$f(\epsilon) = n_0 \Lambda^3 e^{-\epsilon/kT} \Theta\left(\epsilon_t - \epsilon\right) \tag{4.11}$$

where ϵ_t is the trap depth, Θ is the Heaviside step function and $n_0\Lambda^3$ is a normalization constant depending on the total number of particles. The physical interpretation of this expression is straightforward - any particle with energy higher than ϵ_t is assumed to instantly leave the trap. The final piece of the puzzle is the density of states (DoS) in the trap given by:

$$\rho(\epsilon) \equiv (2\pi\hbar)^{-3} \int d^3r d^3p \delta\left(\epsilon - U(\mathbf{r}) - p^2/2m\right) = \frac{2\pi(2m)^{3/2}}{(2\pi\hbar)^3} \int_{U(\mathbf{r})\leq\epsilon} d^3r \sqrt{\epsilon - U(\mathbf{r})} \tag{4.12}$$

Note that $\rho(\epsilon)$ is solely determined by the shape of the trap $U(\mathbf{r})$. We are now armed with a set of expression that will allow us to compute all the relevant thermodynamical quantities. For example, substituting $\epsilon = p^2/2m + U(\mathbf{r})$ into equation 4.11 and integrating over momentum yields the density of particles in the trap $n(r) = n_0 exp(-\beta U(\mathbf{r}))P(3/2, \kappa)$ where P is the normalized incomplete gamma function[4] and $\kappa = \beta(\epsilon_t - U(\mathbf{r}))$. By defining the partition function:

[3] This is valid in the low temperature regime reached at the end of the MOT stage [88]

[4] $P(a, \eta) \equiv \frac{1}{\Gamma(a)} \int_0^\eta dt t^{a-1} e^{-t}$

$$\zeta = \int_0^{\epsilon_t} d\epsilon \rho(\epsilon) \exp(-\epsilon/kT) \tag{4.13}$$

and using the normalization condition for the total number of particles N we arrive at the expression for $n_0\Lambda^3 = N/\zeta$. Other thermodynamic quantities such as the total energy $E = \int d\epsilon\epsilon\rho(\epsilon)f(\epsilon)$, the heat capacity $C = \frac{\partial E}{\partial T}$ or chemical potential $\mu = \frac{\partial E}{\partial N}$ follow naturally.

As particles move around in the trap they scatter off each other. In some of these event a particle can end up being scattered into a state with $\epsilon > \epsilon_t$ resulting in loss of that particle and the energy it was carrying. This is the mechanism of evaporation. By integrating over the empty states outside of the trap and the rate at which they get populated one can derive an expression for the total particle and energy loss due to evaporation:

$$\dot{N}_{\text{ev}} = -\int_{\epsilon_t}^{\infty} d\epsilon \rho\left(\epsilon\right) \dot{f}\left(\epsilon\right) = \dot{N}_{\text{ev}} = -n_0^2 \sigma \bar{v} e^{-\eta} V_{\text{ev}} \tag{4.14}$$

$$V_{\text{ev}} = \frac{\Lambda^3}{kT} \int_0^{\epsilon_t} d\epsilon \rho(\epsilon) \left[\left(\epsilon_t - \epsilon - kT\right) e^{-\epsilon/kT} + kT e^{-\eta}\right] \tag{4.15}$$

$$\dot{E}_{\text{ev}} = -\int_{\epsilon_t}^{\infty} d\epsilon\epsilon \rho\left(\epsilon\right) \dot{f}\left(\epsilon\right) = \dot{N}_{\text{ev}} \left\{\epsilon_t + \frac{V_{\text{ev}} - X_{\text{ev}}}{V_{\text{ev}}} kT\right\} \tag{4.16}$$

$$X_{\text{ev}} = \frac{\Lambda^3}{kT} \int_0^{\epsilon_t} d\epsilon \rho(\epsilon) \left[kT e^{\epsilon/kT} - \left(\epsilon_t - \epsilon + kT\right) e^{\eta}\right] \tag{4.17}$$

here σ is the s-wave scattering cross section [115, 88] and $\bar{v} = (8kT/\pi m)^{1/2}$ is the characteristic velocity of an atom in the cloud.

Finally, by treating the total energy as a function of N and T only we can write the total energy differential as $dE = \frac{\partial E}{\partial T} dT + \frac{\partial E}{\partial N} dN$. By dividing by dt and acknowledging that the partial derivatives correspond to the heat capacity and chemical potential one can derive an equation for the time evolution of temperature:

$$\dot{T} = \frac{\dot{E} - \mu \dot{N}}{C} \tag{4.18}$$

Numerically solving this equation for T and N in small time increments yields the whole time evolution of the system. Note that in the current formulation of the problem, an optimal solution would be an infinitely deep trap with a diverging evaporation time. This is because the lack of time constraint makes waiting for an extremely improbable collision that will take away most of the cloud's energy worth the time. In reality, there are processes that cause particle loss and heating independent of the trap depth. Three major contributors are collisions with residual gas in the vacuum chamber, 3-body collisions [116] between trapped particles and off-resonant light scattering with the trapping beam. In the case of our experiment, the first contributor limits the lifetime of the trapped atomic cloud to ≈ 40s which is much longer than the typical decay time due to 3-body collisions. It will therefore be omitted from the following discussion.

The 3-body loss rate is governed by the equation $\frac{dn}{dt} = -L_3 n^3$ here n is the particle density and L_3 is the 3-body loss coefficient that depends on the species and possibly on an external magnetic field [117]. Assuming that the probability of

3-body recombination is independent of the energy of the particles involved in it, the total energy loss due to this process per unit volume is simply the number of particles lost from this volume times the average energy per particle in this volume. This can be expressed as $dE_{3b} = dN_{3b}\bar{E}(r)$ where $dN_{3b} = -L_3 n^3(r) dV dt$ and:

$$\bar{E}(r) = \frac{\int \epsilon(r,p) f(r,p) d^3p}{\int f(r,p) d^3p} = U(r) + \frac{3}{2}kT\frac{P(5/2,\kappa)}{P(3/2,\kappa)} \tag{4.19}$$

Note that in the limit of an infinitely deep trap $\bar{E}(r) \to U(r)+3/2kT$ as expected. We can express the total rate of change of particle number and energy due to 3-body collisions as:

$$\dot{N}_{3b} = -L_3 \int n^3(r) d^3r \tag{4.20}$$

$$\dot{E}_{3b} = -L_3 \int n^3(r) \bar{E(r)} d^3r \tag{4.21}$$

Note that because of the cubic dependence on the density, atoms are preferentially removed from the center of the trap and so the averaged energy removed by a three-body collision is smaller than the average energy per atom in the trap. Consequently, three-body collisions cause *heating* of the trapped gas in addition to particle loss.

The second type of heating mechanism that we will discuss is the off-resonant light scattering. Equation 4.2 gives the expression for the scattering rate in terms of the imaginary polarization and local intensity. The intensity prefactor was calculated using the method described in section 4.2 and its value is $C_\Gamma = 1.79\dot{1}0^{-10} J^{-1}m^2$. So the scattering rate for an atom at position r is $\Gamma(r) = C_\Gamma I(r)$. If we assume that an atom's energy increases by twice the photon recoil energy $E_r = \frac{(\hbar k)^2}{2m}$ because of the absorption and subsequent re-emission then the heating rate of the cloud is given by:

$$\dot{E}_\Gamma = 2\frac{(\hbar k)^2}{2m}\int \Gamma(r) n(r) d^3r = C_\Gamma \frac{(\hbar k)^2}{m}\int I(r) n(r) d^3r \tag{4.22}$$

So far, all the effects that we have considered assume a fixed trap depth or more generally a stationary trap. However, during forced evaporation the trap depth (RF knife, ODT) as well as the trap shape (ODT only) can change which in return affects other thermodynamical quantities such as the particle number N and the temperature T. This is where the the literature is no longer coherent in the formulation of the problem. For the case of an RF knife evaporation, the situation is still simple enough. Here ϵ_t is no longer a fixed quantity but a variable. As the trap depth is lowered, energy eigenstates at the very edge of the trap i.e. at $\epsilon \approx \epsilon_t$ suddenly appear out of the trap and are irreversibly lost. This effect is called *spilling* and the corresponding particle and energy loss can be simply calculated by considering the density of states at the trap edge, their average occupation number and the rate at which the trap is lowered:

$$\dot{N}_{spill} = f(\epsilon_t)\rho(\epsilon_t)\dot{\epsilon_t} = \frac{N}{\zeta} e^{-\beta\epsilon_t}\rho(\epsilon_t)\dot{\epsilon_t} \tag{4.23}$$

$$\dot{E}_{spill} = \dot{N}_{spill}\epsilon_t \tag{4.24}$$

Since the trap depth is now considered a variable, we need to change our expression for the total energy differential $dE = \frac{\partial E}{\partial T}dT + \frac{\partial E}{\partial N} + \frac{\partial E}{\partial \epsilon_t}d\epsilon_t$ which gives for the time derivative of temperature:

$$\dot{T} = \frac{\dot{E} - \mu\dot{N} - Q\dot{\epsilon_t}}{C} \tag{4.25}$$

where $Q = \frac{\partial E}{\partial \epsilon_t}$, $\dot{E} = \dot{E}_{ev} + \dot{E}_{3b} + \dot{E}_{\Gamma} + \dot{E}_{spill}$ and $\dot{N} = \dot{N}_{ev} + \dot{N}_{3b} + \dot{N}_{spill}$. It turns out that all the terms coming from spilling cancel out in equation 4.25 which means that spilling has no effect on the temperature. However, it still contributes to the particle loss alongside three-body collisions and evaporation.

Intuitively, changing the shape of the trap should result in heating and change of the total energy in a similar manner to doing work on a gas by compressing/relaxing it. Pinkse et al. [118] (equations 14, 47, 48) calculate this change by considering the expression for entropy derived from the Helmholtz free energy. By taking the differential of the entropy one can express its time evolution as a function of $\dot{E}$. Rearranging this expression and calculating the entropy per particle lost due to trap relaxation/squeezing leads to the final expression for the change in energy which can, in return, be used in equation 4.25 to obtain the change in temperature. Berg-Sorensen [114] uses a different approach in which an explicit expression for the time evolution of the trapping potential $U = U(\boldsymbol{r}, t)$ is used to calculate the corresponding change in total energy and particle number. We present yet another angle of approach in which we calculate the total change in energy due to an adiabatic change of the potential and we combine it with the spilling terms derived above (equation 4.23) to arrive at the final set of differential equations.

We express the entropy $S = \frac{E-F}{T}$ where $F = -kTln(\frac{\zeta^N}{N!})$ is the Helmholtz free energy. By taking the total differential and setting it to 0 i.e. adiabatic change and by assuming that there are no particles lost in the process ($dN = 0$) we arrive at the expression for change in energy:

$$\dot{E}_P = -kT\frac{N}{\zeta}\dot{P}\int e^{-\beta\epsilon}\frac{\partial\rho}{\partial P}d\epsilon \tag{4.26}$$

here P is a trap parameter. For an ODT the most natural choice is the power in the beam(s). All that is left is to acknowledge that the quantity $Q = \frac{\partial E}{\partial \epsilon_t}$ will now also contain extra expressions that contain terms of the form $\frac{\partial \rho}{\partial P}$ as a result of the trap changes:

$$Q = Q_{spill} + \frac{N}{\zeta}\left(\int \epsilon e^{-\beta\epsilon}\frac{\partial\rho}{\partial P}d\epsilon - \mu\int e^{-\beta\epsilon}\frac{\partial\rho}{\partial P}d\epsilon\right) \tag{4.27}$$

A simulation was written in Python to solve the system of differential equations describing evaporation in the crossed-beam dipole trap geometry implemented in our group. A 3D box with specified dimensions is defined and partitioned into smaller regions of space such that $U_{dip} \approx const.$ within that region. The dimensions of the box are different in all three directions because of the tighter confinement along the y axis as defined in figure 4.3 as opposed to weaker confinement along the ODT beams. The dipole potential is calculated at each point on the grid as is the total potential depth (eq.4.6). The energy interval $(0, \epsilon_t)$ is split evenly into adjustable number of bins and by carrying integration in 3D space based on equation 4.12 the density of states $\rho(\epsilon)$ is calculated at each energy point defined by the interval.

From that, all the relevant quantities can be calculated including the particle density $n(r)$. We use the average particle density $\bar{n}$ to calculate the average scattering time $t_{scatt} = \frac{1}{\sigma \bar{n}} \sqrt{\frac{\pi m}{16kT}}$. This characteristic time multiplied by a variable integer α is then used as the time step in the numerical integration. Literature suggests [110] that an average of ≈ 3 scattering events is required for the gas to thermalize so as a lower bound for α we use the value of 3.

We ran a simulation in which ODT1 is ramped linearly from its initial power of 25 W down to 5 W over the course of 1 second. The tree different models for the terms involving the trap shape changes based on [118], [114] and our calculations were used for comparison. The results are shown in figure 4.7. The method described by Berg-Sorensen [114] (orange) deviates from that used by Pinkse et al. [118] (blue) and from our calculations (green) which are both in good agreement with each other. The main difference can be seen in particle loss which is then reflected in the phase space density (PD). Note that the initial PD was $7.4 \cdot 10^{-4}$ whereas the final one was an order of magnitude larger. Having found good agreement with established literature we can now use our simulation as a starting point for optimizing the evaporation ramp.

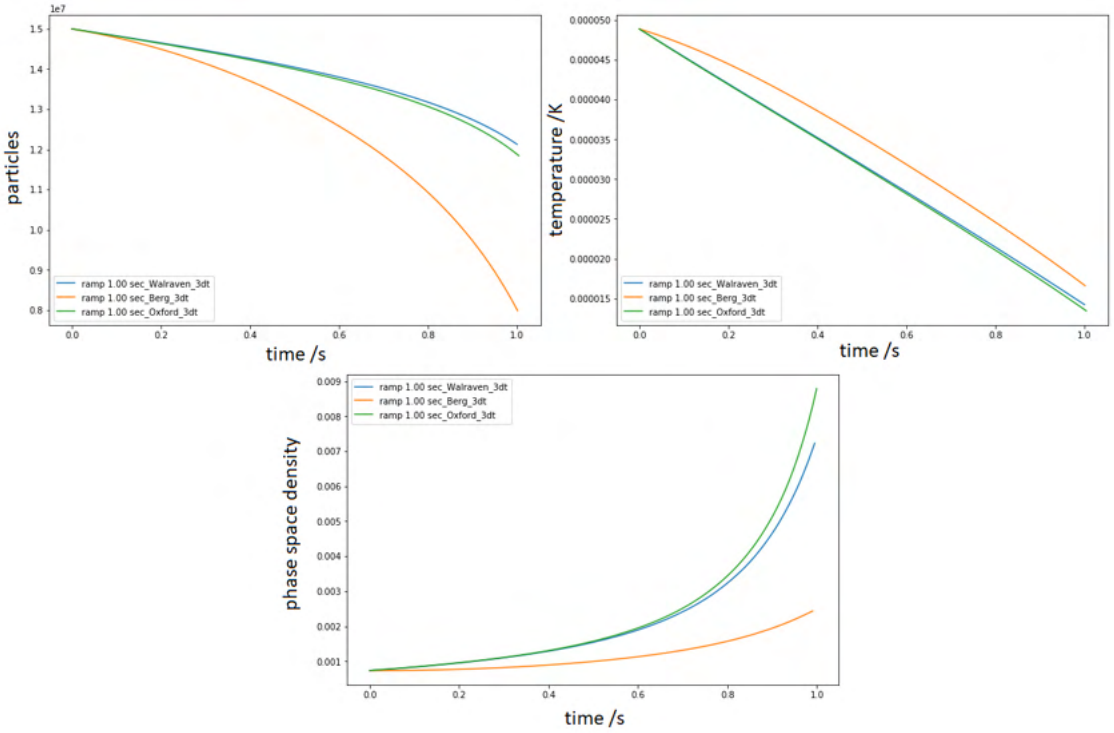

Figure 4.7 – Comparison of evaporation models. Data from a simulation of an evaporation ramp during which the power of ODT1 was reduced linearly from 25 W to 5 W over one second while ODT2 was kept at 5 W. Model from [118] (blue) is in good agreement with our model (green) whereas model from [114] (orange) deviates slightly. Note the ten-fold increase in phase space density.

The evaporation simulations are still at an early stage but show some promising results. One of the greatest challenges as with any computer simulation is minimization of the computational cost without lowering the accuracy of the results. In our case, it is the choice of the time step, the size of the box and the frequency at which the energy space is sampled for the density-of-states calculations. The

long tails of the ODT along the beams make the system somewhat sensitive to the choice of box dimensions along those directions. An alternative treatment of the wing distributions exists [119] and will be the subject of future research. The lack of analytic expressions for the thermodynamic quantities in case of the crossed-beam ODT can possibly be circumvented once the evaporation has reached a stage when the power in the two beams is comparable. At that point, the harmonic approximation is very good and more importantly analytically solvable, saving precious computational time. As can be seen from the equations discussed in this chapter, some of the expressions rely on the knowledge of the scattering cross section σ or the three-body recombination constant L_3. Neither of these is readily accessible for the case of Erbium. In the future, we plan to conduct our own measurements of these quantities to improve the accuracy of the evaporation model. Furthermore, there is more advanced literature available [120, 121] on the topic of evaporation that will hopefully provide more insight into utilizing the already existing simulation for optimizing our evaporation ramp. If time permits, a comparison of our thermodynamics method with the molecular dynamics method [111, 106, 110] could be done to properly assess the benefits and shortcomings of both approaches.

Chapter 5

Outlook

5.1 Project timeline

Bellow is an approximate timeline of the project for the near future. It mainly consists of technical milestones that need to be reached in order to be able to meet the experimental goals outlined in section 1.1 and section 5.2.

- 1 - 15 September 2021: Finish ZS and MOT optimization
- 16 - 30 September 2021: Optimize ODT loading + finish K D1 and D2 optics
- October 2021: Optimize evaporation ramp using simulation and experimental data + finish building K vacuum extension including a three week bake out
- November 2021: Reach BEC of Er + start characterizing K 2D+ MOT
- December 2021 - January 2022: Set up optical transport stage to science cell + optimize K 2D+ MOT
- February - March 2022: Create optical box potential using SLM + obtain and optimize K 3D MOT
- April - June 2022: Characterize Er, K and interspecies Feschbach resonances, optimize dual species evaporation, transport and trapping
- July 2022 onwards: Proceed with planned research

Note that the Er and K parts of the experiment are, to a certain extent, decoupled and can advance at different rates. Certain phenomena such as the roton excitation spectrum [57, 58] or supersolidity [64, 65, 66] can be investigated once the BEC and box trap stage of Erbium is reached regardless of the state of the Potassium setup. In the following section we will briefly touch on a few projects that we plan to pursue immediately after all the essential experimental stages have been reached.

5.2 Future experiments

Once we achieve Bose-Einstein condensation in Erbium we plan to transport it to a glass science cell and trap it in a quasi-2D circular box potential [23]. The box

potential will be realised by overlapping a blue-detuned (372 nm) repulsive hollow cylindrical beam with a red-detuned (1030nm) attractive flat sheet beam creating a "pancake-like" trap (see figure 5.1 left). The shaping of the repulsive beam will be done using a Spatial Light Modulator (SLM). Once the condensate is confined in this geometry, we will proceed with characterizing its excitation spectrum. It has been predicted and observed [57, 58, 59] (albeit in a quasi-1D geometry) that the excitation spectrum should show a characteristic softening of the Bogoliubov dispersion. This can be explained by taking into account the anisotropy of the diople-dipole interaction. When the dipoles are aligned and pointed out of the plane of the trap, the DDI is mainly repulsive. However, an excitation with high enough wavenumber will bring the dipoles into an attractive configuration by displacing them out of the plane of the trap relative to each other (see figure 5.1 right). This results in lowering of the energy of the system and hence a roton minimum in the excitation spectrum. Furthermore, it is believed that roton instability is responsible for the formation of supersolid phase of matter [66, 65]. Our novel trap shape will allow us to investigate this phenomenon in quasi-2D geometries.

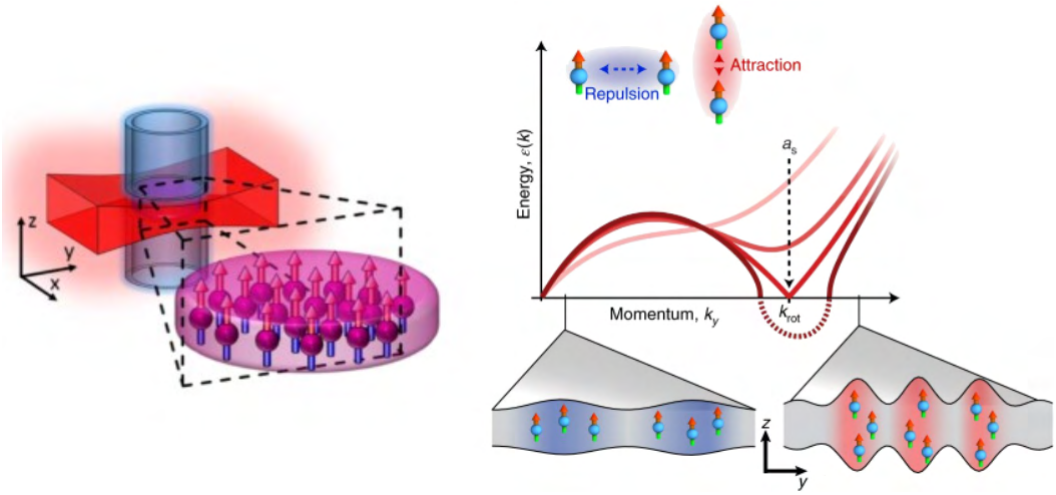

Figure 5.1 – 2D box trap and rotons. (Left) Cartoon of our planned realisation of a quasi-2D homogeneous box trap. A red detuned sheet beam will tightly confine the atoms in the z direction whereas a blue detuned cylindrical beam will create a circular boundary of the trap. By applying magnetic field we can control the direction of the Erbium dipoles and hence their interaction strength. (Right) Expected form of the excitation spectrum of a dipolar BEC. The anisotropy of the DDI is responsible for softening of the excitation spectrum at lower wavelengths due to favourable alignment of the dipoles. Right figure taken from [59].

Addition of Potassium will open up a range of possibilities for the study of impurity physics. Our initial interest will be focused on the investigation of Bose polarons [72, 70, 71]. A polaron is a quasiparticle that arises from interactions of an impurity with background bath of particles. As the impurity moves through the background it distorts its surroundings. For an outside observer, the system of impurity-distortions (phonons in case of bosonic bath) displays properties of a single particle with an effective mass and mobility through the medium that is different from that of the impurity. Perhaps the most well-known example of a polaron is an electron moving through a lattice. It is believed that polaron-polaron interactions play a crucial role in the formation of Cooper pairs that are responsible for the

phenomenon of superconductivity [122]. We will be able to simulate such systems with our setup with an added twist. Due to the DDI between Erbium atoms, the phonon spectrum of the bath is anisotropic [123]. The dressing of the K impurity by the Er phonons will therefore lead to *anisotropic polarons* [84] with different effective mass in different directions. Furthermore, roton excitations can also contribute to the dressing of the impurity. By tuning the Er-K interaction via an interspecies Feshbach resonance and by independently tuning the DDI between Er atoms [82, 81] we can fully explore all the polaronic regimes. RF spectroscopy will be used to excite the polarons and hence measure their energy and lifetime whereas species-selective optical gradient will be used to apply force to the impurities and, by tracking their center-of-mass motion, measure their mass in different directions.

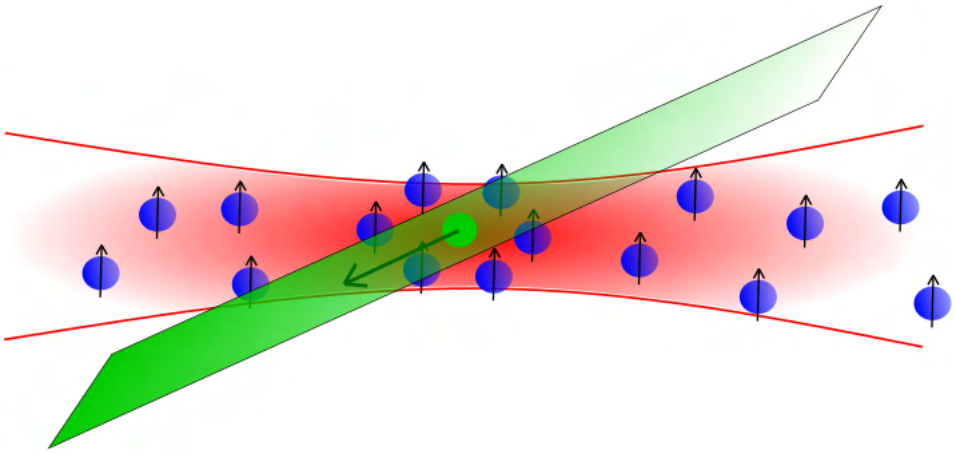

Figure 5.2 – A cartoon of a polaron in dipolar bath. By applying a selective optical potential we can exert a force on the impurity without disturbing the Erbium bath. In practice this would be achieved by using light at a wavelength where the Er polarizability is close to zero.

Another experimental direction where the impurity plays a pivotal role concerns the flow of quantum information in an open system. Generally, random interactions of a qubit with its environment are responsible for the loss of coherence and hence information from the system. Such behaviour is called Markovian and has been a thorn in the eye for all the physicists trying to experimentally realise a quantum computer. Recently, there has been an increased interest in the so-called non-Markovian systems where a backflow of information from the environment back to the qubit is possible [85, 86, 124, 125]. It has been proposed [87, 126] that a qubit in a 2D dipolar bath can be used to realise such system thanks to the roton feature in the excitation spectrum (see above). With its high degree of tunability and the desired geometry, our experimental setup will be ideal for exploring this area. Furthermore, both the analysis of polarons and manipulation of Potassium qubits require similar experimental techniques such as applying RF pulses [127] making this combination of research topics particularly attractive from the experimental standpoint.

Appendix A

Minor projects

A.1 Magnetometer

A high precision magnetometer was constructed to investigate the possibility of magnetic field fluctuations in the MOT chamber. It consists of an HMC2003 3-axis magnetic sensor and an OpAmp potential divider stage which feeds the signal from the three axes directly into an Arduino Duo. The Arduino takes several hundred samples in a short time and averages the signal to reduce the digitization error. It then sends the data via serial connection to a PC where it is analyzed using a simple Python script. Figure A.1 shows the schematic of the circuit.

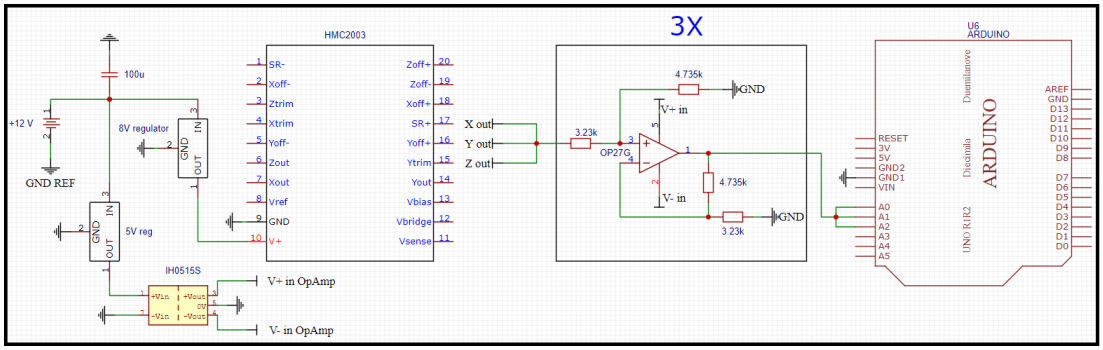

Figure A.1 – Schematic of the magnetometer circuit. The whole system is powered directly from mains and shares a common ground with the Arduino controller. For clarity, the wiring of the sensor to the potential divider stage is not shown and is simply replaced by the corresponding axes pins. The output of the potential divider goes into an analog channel pin on the Arduino. For simplicity, the outputs were merged into one but in reality there is a separate output for each axis.

The sensitivity of the sensor is 1G/V which, together with the potential divider and 12-bit sampling of the Arduino, yields the final resolution of 1.2mG. It was suspected that an induced magnetization on the vacuum chamber could be responsible for instability of the MOT. The magnetometer was therefore placed a few centimeters above the chamber and logging of the sensor data was triggered at a specific point during the experimental sequence right after all the coils were turned off for the cool-down phase. Should some induced magnetization be present we would expect to observe a decaying signal as the material slowly demagnetizes. Data from a few experimental runs is shown in figure A.2.

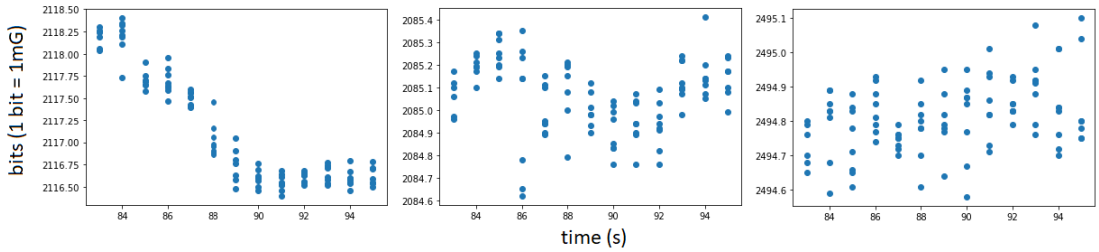

Figure A.2 – Magnetometer data from a typical run. The three figures show data collected from the three axis of the magnetometer over the course of a single experimental run. The x-axis shows time in seconds (note that a random run was chosen from a series of runs and hence the time axis doesn't start at 0 but at the time when that particular run started). The y axis shows the digitized analogue reading from the Arduino where each unit corresponds to ≈ 1.2 mG. We see that the value of the field oscillates well within the digitization error of one unit and so the magnetometer, at least with its current resolution, doesn't confirm the presence of any magnetization effects.

This did not show any decaying trends and was therefore inconclusive. It later turned out that the source of jitter in the MOT cloud position was a faulty mirror (see section 2.3). Future plans with the magnetometer involve using it as an active element in compensating stray fields around the optical table.

A.2 Thermometer

A five channel thermometer was created for the purpose of monitoring the temperature during the bake out of the potassium vacuum setup (see section 3.3). Type K, class 1 thermocouple is used as the temperature gauge with the signal being amplified via a non-inverting OpAmp configuration and read off by an Arduino Uno device. After processing the signal and converting it to a temperature value based on previous calibration (see below), the data is transferred to a PC via serial connection and a logging software developed by a member of our group is used to store and plot the data. Furthermore, an LCD display connected to the Arduino displays real time temperature reading from one of the channels allowing for immediate measurements. The schematic of the circuitry is shown in figure A.3.

The temperature readings are calibrated by using two reference objects at a known temperature and the knowledge that the thermocouple is sufficiently linear in the range of temperatures that we are interested in (20° - 120°C). For reference, we use a medical thermometer to read off my body temperature and a retail thermometer to measure the temperature of a controllable hot plate set to ≈ 150°C. The accuracy achievable with this calibration and by averaging over many readings to reduce the digitization error is $\approx \pm 1$°C at 120°C which will be the target bake out temperature. This is more than sufficient for the intended application. To test the thermometer and find out whether we can heat the potassium sample to the desired temperatures we placed a 3D printed copy of the K sample ampoule into the bellow section (see figure 3.9). The five thermometer probes were placed alongside the inner surface of the bellow and the bellow was gradually heated up using simple heating wire (see figure A.4 left). The temperature was logged via the Arduino and the obtained data is shown in figure A.4 right. The yellow and gray traces are

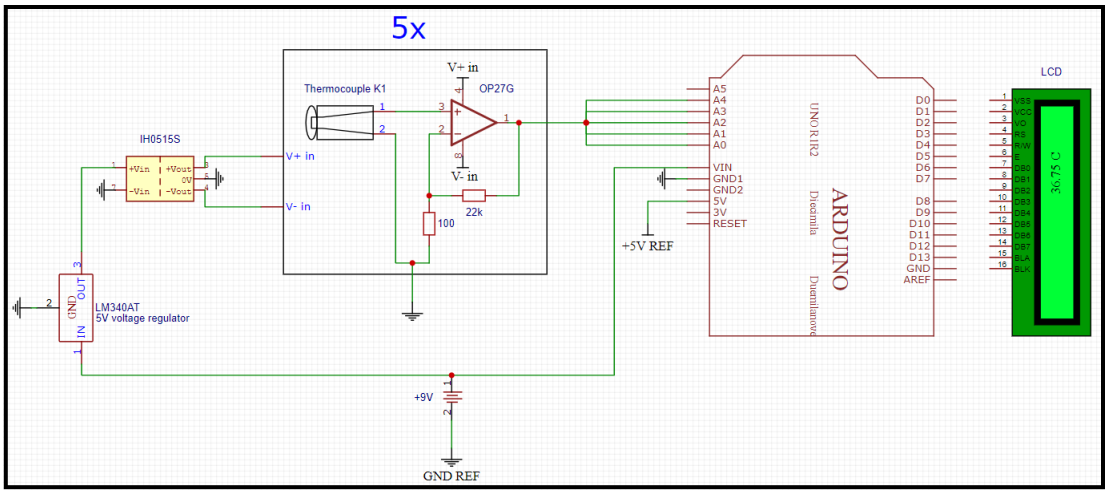

Figure A.3 – Schematic of the thermometer circuit. All the circuitry is housed in a plastic box that has 9V input socket and a knob to control the contrast of the LCD. Each of the thermocouples has a separate amplifying stage that is then fed into an analog channel of the Arduino. For simplicity, these output/input wires were merged into one but in reality there is one for each channel. The wiring of the Arduino to the LCD is described in [128]

from the probes that were in direct contact with the ampoule and show that we can comfortably heat the ampule above the 70°C threshold without reaching the current limitations of the wire which is sufficient for the experimental procedure.

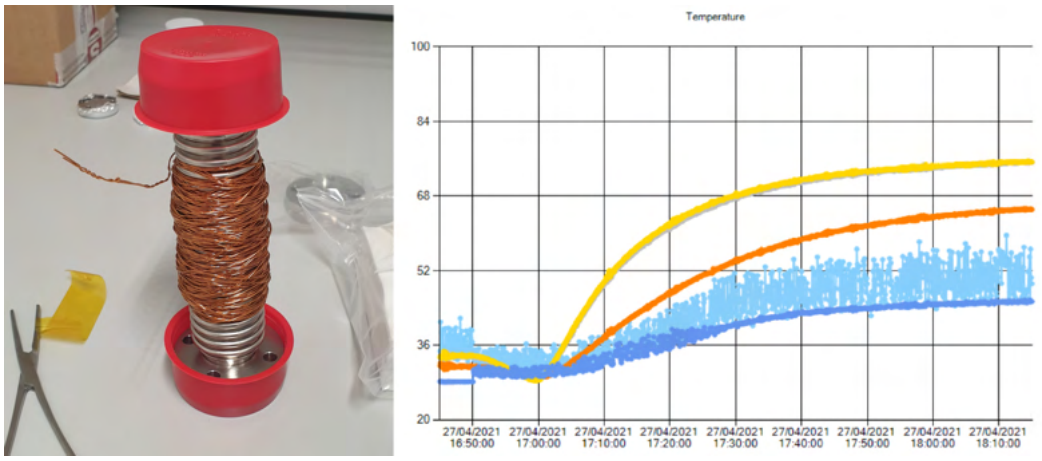

Figure A.4 – Heating of the bellow. (Left) The atomic bellow wrapped in heating wire. The bellow is bendable so that when the K glass ampoule is inserted into it, it can be broken by bending the bellow without having to invade the vacuum. (Right) A plot of temperature as collected by the five thermometer channels that were situated alongside the inner surface of the bellow. The blue traces are from the channels located at the top and bottom end of the bellow with the light blue trace being at the top. The fluctuations in the temperature can be explained be turbulences forming as the hot air rose through the chimney-like structure. The yellow and gray (overlapped by yellow) traces were closest to the 3D printed ampoule and are therefore most reflective of the temperatures that will be attainable in the real experiment. Steady state at $\approx 70°$C was reached after an hour.

Bibliography

[1] R Gordon Gould et al. "The LASER, light amplification by stimulated emission of radiation". In: *The Ann Arbor conference on optical pumping, the University of Michigan*. Vol. 15. 128. 1959, p. 92.

[2] Steven Chu et al. "Three-dimensional viscous confinement and cooling of atoms by resonance radiation pressure". In: *Physical review letters* 55.1 (1985), p. 48.

[3] Mike H Anderson et al. "Observation of Bose-Einstein condensation in a dilute atomic vapor". In: *science* 269.5221 (1995), pp. 198–201.

[4] Kendall B Davis et al. "Bose-Einstein condensation in a gas of sodium atoms". In: *Physical review letters* 75.22 (1995), p. 3969.

[5] Brian DeMarco and Deborah S Jin. "Onset of Fermi degeneracy in a trapped atomic gas". In: *science* 285.5434 (1999), pp. 1703–1706.

[6] Jean Dalibard and Claude Cohen-Tannoudji. "Laser cooling below the Doppler limit by polarization gradients: simple theoretical models". In: *JOSA B* 6.11 (1989), pp. 2023–2045.

[7] Wolfgang Ketterle and NJ Van Druten. "Evaporative cooling of trapped atoms". In: *Advances in atomic, molecular, and optical physics* 37 (1996), pp. 181–236.

[8] Matthias Weidemüller et al. "A novel scheme for efficient cooling below the photon recoil limit". In: *EPL (Europhysics Letters)* 27.2 (1994), p. 109.

[9] D Boiron et al. "Three-dimensional cooling of cesium atoms in four-beam gray optical molasses". In: *Physical Review A* 52.5 (1995), R3425.

[10] MR Tarbutt. "Laser cooling of molecules". In: *Contemporary Physics* (2019).

[11] Lincoln D Carr et al. "Cold and ultracold molecules: science, technology and applications". In: *New Journal of Physics* 11.5 (2009), p. 055049.

[12] ES Shuman et al. "Radiative force from optical cycling on a diatomic molecule". In: *Physical review letters* 103.22 (2009), p. 223001.

[13] Cindy A Regal et al. "Creation of ultracold molecules from a Fermi gas of atoms". In: *Nature* 424.6944 (2003), pp. 47–50.

[14] Milan Krstajic. "Experimental Platform for a Box-Trapped Dipolar Quantum Gas". In: (2021).

[15] Richard P Feynman. "Simulating physics with computers". In: *Feynman and computation*. CRC Press, 2018, pp. 133–153.

[16] G Gauthier et al. “Direct imaging of a digital-micromirror device for configurable microscopic optical potentials”. In: *Optica* 3.10 (2016), pp. 1136–1143.

[17] David McGloin et al. “Applications of spatial light modulators in atom optics”. In: *Optics Express* 11.2 (2003), pp. 158–166.

[18] Markus Greiner et al. “Quantum phase transition from a superfluid to a Mott insulator in a gas of ultracold atoms”. In: *nature* 415.6867 (2002), pp. 39–44.

[19] Alain Aspect and Massimo Inguscio. “Anderson localization of ultracold atoms”. In: *Phys. Today* 62.8 (2009), p. 30.

[20] L Fallani et al. “Ultracold atoms in a disordered crystal of light: Towards a Bose glass”. In: *Physical review letters* 98.13 (2007), p. 130404.

[21] Gregor Jotzu et al. “Experimental realization of the topological Haldane model with ultracold fermions”. In: *Nature* 515.7526 (2014), pp. 237–240.

[22] Monika Aidelsburger et al. “Realization of the Hofstadter Hamiltonian with ultracold atoms in optical lattices”. In: *Physical review letters* 111.18 (2013), p. 185301.

[23] Alexander L Gaunt et al. “Bose-Einstein condensation of atoms in a uniform potential”. In: *Physical review letters* 110.20 (2013), p. 200406.

[24] Christoph Eigen et al. “Observation of weak collapse in a Bose-Einstein condensate”. In: *Physical Review X* 6.4 (2016), p. 041058.

[25] Nir Navon et al. “Emergence of a turbulent cascade in a quantum gas”. In: *Nature* 539.7627 (2016), pp. 72–75.

[26] Michael Robin Matthews et al. “Vortices in a Bose-Einstein condensate”. In: *Physical Review Letters* 83.13 (1999), p. 2498.

[27] Jamil R Abo-Shaeer et al. “Observation of vortex lattices in Bose-Einstein condensates”. In: *Science* 292.5516 (2001), pp. 476–479.

[28] Jérôme Beugnon and Nir Navon. “Exploring the Kibble–Zurek mechanism with homogeneous Bose gases”. In: *Journal of Physics B: Atomic, Molecular and Optical Physics* 50.2 (2017), p. 022002.

[29] I-K Liu et al. “Dynamical equilibration across a quenched phase transition in a trapped quantum gas”. In: *Communications Physics* 1.1 (2018), pp. 1–12.

[30] CA Regal and DS Jin. “Experimental realization of the BCS-BEC crossover with a Fermi gas of atoms”. In: *Advances In Atomic, Molecular, and Optical Physics* 54 (2007), pp. 1–79.

[31] Toshiya Kinoshita, Trevor Wenger, and David S Weiss. “Observation of a one-dimensional Tonks-Girardeau gas”. In: *Science* 305.5687 (2004), pp. 1125–1128.

[32] Guillaume Lang. *Correlations in low-dimensional quantum gases*. Springer, 2018.

[33] J Steinhauser. “Observation of quantum Hawking radiation and its entanglement in an analogue black hole”. In: *Nature Physics* 12 (2016), pp. 959–965.

[34] Javier Rodrıguez-Laguna et al. "Synthetic Unruh effect in cold atoms". In: *Phys. Rev. A* 95 (1 Jan. 2017), p. 013627. DOI: 10.1103/PhysRevA.95.013627. URL: https://link.aps.org/doi/10.1103/PhysRevA.95.013627.

[35] S Bize et al. "Cold atom clocks and applications". In: *Journal of Physics B: Atomic, molecular and optical physics* 38.9 (2005), S449.

[36] Marco Schioppo et al. "Ultrastable optical clock with two cold-atom ensembles". In: *Nature Photonics* 11.1 (2017), pp. 48–52.

[37] Sean Ravenhall, Benjamin Yuen, and Chris Foot. "High-flux, adjustable, compact cold-atom source". In: *Optics Express* 29.14 (2021), pp. 21143–21159.

[38] N Poli et al. "A transportable strontium optical lattice clock". In: *Applied Physics B* 117.4 (2014), pp. 1107–1116.

[39] Jacopo Grotti et al. "Geodesy and metrology with a transportable optical clock". In: *Nature Physics* 14.5 (2018), pp. 437–441.

[40] Christian Freier et al. "Mobile quantum gravity sensor with unprecedented stability". In: *Journal of Physics: Conference Series*. Vol. 723. 1. IOP Publishing. 2016, p. 012050.

[41] Peter W Graham et al. "New method for gravitational wave detection with atomic sensors". In: *Physical review letters* 110.17 (2013), p. 171102.

[42] Savas Dimopoulos et al. "Atomic gravitational wave interferometric sensor". In: *Physical Review D* 78.12 (2008), p. 122002.

[43] Ta-You Wu and Takashi Ohmura. *Quantum theory of scattering*. Courier Corporation, 2014.

[44] S Inouye et al. "Observation of Feshbach resonances in a Bose–Einstein condensate". In: *Nature* 392.6672 (1998), pp. 151–154.

[45] Ph Courteille et al. "Observation of a Feshbach resonance in cold atom scattering". In: *Physical Review Letters* 81.1 (1998), p. 69.

[46] Richard J Fletcher et al. "Stability of a unitary Bose gas". In: *Physical review letters* 111.12 (2013), p. 125303.

[47] Philip Makotyn et al. "Universal dynamics of a degenerate unitary Bose gas". In: *Nature Physics* 10.2 (2014), pp. 116–119.

[48] Thierry Lahaye et al. "The physics of dipolar bosonic quantum gases". In: *Reports on Progress in Physics* 72.12 (2009), p. 126401.

[49] Mikhail A Baranov. "Theoretical progress in many-body physics with ultracold dipolar gases". In: *Physics Reports* 464.3 (2008), pp. 71–111.

[50] Steven A Moses et al. "New frontiers for quantum gases of polar molecules". In: *Nature Physics* 13.1 (2017), pp. 13–20.

[51] K-K Ni et al. "A high phase-space-density gas of polar molecules". In: *science* 322.5899 (2008), pp. 231–235.

[52] Tetsu Takekoshi et al. "Ultracold dense samples of dipolar RbCs molecules in the rovibrational and hyperfine ground state". In: *Physical review letters* 113.20 (2014), p. 205301.

[53] Emily Altiere et al. “Dipole-dipole interaction between rubidium Rydberg atoms”. In: *Physical Review A* 84.5 (2011), p. 053431.

[54] Axel Griesmaier et al. “Bose-Einstein condensation of chromium”. In: *Physical Review Letters* 94.16 (2005), p. 160401.

[55] Mingwu Lu et al. “Strongly dipolar Bose-Einstein condensate of dysprosium”. In: *Physical review letters* 107.19 (2011), p. 190401.

[56] K Aikawa et al. “Bose-Einstein condensation of erbium”. In: *Physical review letters* 108.21 (2012), p. 210401.

[57] RP Feynman and Michael Cohen. “Energy spectrum of the excitations in liquid helium”. In: *Physical Review* 102.5 (1956), p. 1189.

[58] L Santos, GV Shlyapnikov, and M Lewenstein. “Roton-maxon spectrum and stability of trapped dipolar Bose-Einstein condensates”. In: *Physical Review Letters* 90.25 (2003), p. 250403.

[59] Lauriane Chomaz et al. “Observation of roton mode population in a dipolar quantum gas”. In: *Nature physics* 14.5 (2018), pp. 442–446.

[60] D Petter et al. “Probing the roton excitation spectrum of a stable dipolar Bose gas”. In: *Physical review letters* 122.18 (2019), p. 183401.

[61] Holger Kadau et al. “Observing the Rosensweig instability of a quantum ferrofluid”. In: *Nature* 530.7589 (2016), pp. 194–197.

[62] Igor Ferrier-Barbut et al. “Observation of quantum droplets in a strongly dipolar Bose gas”. In: *Physical review letters* 116.21 (2016), p. 215301.

[63] L Chomaz et al. “Quantum-fluctuation-driven crossover from a dilute Bose-Einstein condensate to a macrodroplet in a dipolar quantum fluid”. In: *Physical Review X* 6.4 (2016), p. 041039.

[64] Massimo Boninsegni and Nikolay V Prokof’ev. “Colloquium: Supersolids: What and where are they?” In: *Reviews of Modern Physics* 84.2 (2012), p. 759.

[65] Fabian Böttcher et al. “Transient supersolid properties in an array of dipolar quantum droplets”. In: *Physical Review X* 9.1 (2019), p. 011051.

[66] G Natale et al. “Excitation spectrum of a trapped dipolar supersolid and its experimental evidence”. In: *Physical review letters* 123.5 (2019), p. 050402.

[67] Frédéric Chevy and Christophe Mora. “Ultra-cold polarized Fermi gases”. In: *Reports on Progress in Physics* 73.11 (2010), p. 112401.

[68] André Schirotzek et al. “Observation of Fermi polarons in a tunable Fermi liquid of ultracold atoms”. In: *Physical review letters* 102.23 (2009), p. 230402.

[69] Alexander Cyril Hewson. *The Kondo problem to heavy fermions*. 2. Cambridge university press, 1997.

[70] Zoe Z Yan et al. “Bose polarons near quantum criticality”. In: *Science* 368.6487 (2020), pp. 190–194.

[71] Ming-Guang Hu et al. “Bose polarons in the strongly interacting regime”. In: *Physical review letters* 117.5 (2016), p. 055301.

[72] Nils B Jørgensen et al. "Observation of attractive and repulsive polarons in a Bose-Einstein condensate". In: *Physical review letters* 117.5 (2016), p. 055302.

[73] Norman Mannella et al. "Nodal quasiparticle in pseudogapped colossal magnetoresistive manganites". In: *Nature* 438.7067 (2005), pp. 474–478.

[74] A Lanzara et al. "Evidence for ubiquitous strong electron–phonon coupling in high-temperature superconductors". In: *Nature* 412.6846 (2001), pp. 510–514.

[75] Jozef T Devreese and Alexandre S Alexandrov. "Fröhlich polaron and bipolaron: recent developments". In: *Reports on Progress in Physics* 72.6 (2009), p. 066501.

[76] Davide Dreon et al. "Optical cooling and trapping of highly magnetic atoms: the benefits of a spontaneous spin polarization". In: *Journal of Physics B: Atomic, Molecular and Optical Physics* 50.6 (2017), p. 065005.

[77] E Lucioni et al. "A new setup for experiments with ultracold dysprosium atoms". In: *The European Physical Journal Special Topics* 226.12 (2017), pp. 2775–2780.

[78] Bojeong Seo et al. "Efficient production of a narrow-line erbium magneto-optical trap with two-stage slowing". In: *Physical Review A* 102.1 (2020), p. 013319.

[79] William Lunden et al. "Enhancing the capture velocity of a Dy magneto-optical trap with two-stage slowing". In: *Physical Review A* 101.6 (2020), p. 063403.

[80] Cornelis Ravensbergen et al. "Production of a degenerate Fermi-Fermi mixture of dysprosium and potassium atoms". In: *Physical Review A* 98.6 (2018), p. 063624.

[81] Stefano Giovanazzi, Axel Görlitz, and Tilman Pfau. "Tuning the dipolar interaction in quantum gases". In: *Physical review letters* 89.13 (2002), p. 130401.

[82] Yijun Tang et al. "Tuning the dipole-dipole interaction in a quantum gas with a rotating magnetic field". In: *Physical review letters* 120.23 (2018), p. 230401.

[83] LA Peña Ardila and T Pohl. "Ground-state properties of dipolar Bose polarons". In: *Journal of Physics B: Atomic, Molecular and Optical Physics* 52.1 (2018), p. 015004.

[84] Ben Kain and Hong Y Ling. "Polarons in a dipolar condensate". In: *Physical Review A* 89.2 (2014), p. 023612.

[85] Heinz-Peter Breuer et al. "Colloquium: Non-Markovian dynamics in open quantum systems". In: *Reviews of Modern Physics* 88.2 (2016), p. 021002.

[86] Inés De Vega and Daniel Alonso. "Dynamics of non-Markovian open quantum systems". In: *Reviews of Modern Physics* 89.1 (2017), p. 015001.

[87] Ji-Bing Yuan et al. "Quantum non-Markovian reservoirs of atomic condensates engineered via dipolar interactions". In: *Physical Review A* 95.3 (2017), p. 033610.

[88] Albert Frisch. "Dipolar quantum gases of erbium". In: (2014).

[89] Christopher J Foot et al. *Atomic physics*. Vol. 7. Oxford University Press, 2005.

[90] Theodor W Hänsch and Arthur L Schawlow. "Cooling of gases by laser radiation". In: *Optics Communications* 13.1 (1975), pp. 68–69.

[91] Christopher J Pethick and Henrik Smith. *Bose–Einstein condensation in dilute gases*. Cambridge university press, 2008.

[92] Jabez J McClelland et al. "Bright focused ion beam sources based on laser-cooled atoms". In: *Applied physics reviews* 3.1 (2016), p. 011302.

[93] Jan Hendrik Becher et al. "Anisotropic polarizability of erbium atoms". In: *Physical Review A* 97.1 (2018), p. 012509.

[94] Guillaume Salomon et al. "Gray-molasses cooling of 39K to a high phase-space density". In: *EPL (Europhysics Letters)* 104.6 (2014), p. 63002.

[95] Guillaume Salomon et al. "All-optical cooling of K 39 to Bose-Einstein condensation". In: *Physical Review A* 90.3 (2014), p. 033405.

[96] Hao-Ze Chen et al. "Production of large K 41 Bose-Einstein condensates using D 1 gray molasses". In: *Physical Review A* 94.3 (2016), p. 033408.

[97] Lucas Hofer. "Design and Construction of a Dual Erbium-Potassium Experiment". In: (2019).

[98] K Dieckmann et al. "Two-dimensional magneto-optical trap as a source of slow atoms". In: *Physical Review A* 58.5 (1998), p. 3891.

[99] A Aspect et al. "Laser cooling below the one-photon recoil energy by velocity-selective coherent population trapping". In: *Physical Review Letters* 61.7 (1988), p. 826.

[100] D Rio Fernandes et al. "Sub-Doppler laser cooling of fermionic 40K atoms in three-dimensional gray optical molasses". In: *EPL (Europhysics Letters)* 100.6 (2012), p. 63001.

[101] Paul D Lett et al. "Observation of atoms laser cooled below the Doppler limit". In: *Physical review letters* 61.2 (1988), p. 169.

[102] Jürgen Appel, K-P Marzlin, and AI Lvovsky. "Raman adiabatic transfer of optical states in multilevel atoms". In: *Physical Review A* 73.1 (2006), p. 013804.

[103] Maxence Lepers, J-F Wyart, and Olivier Dulieu. "Anisotropic optical trapping of ultracold erbium atoms". In: *Physical Review A* 89.2 (2014), p. 022505.

[104] Nikolaj Leonidivič Manakov, Vitalij Dmitrievič Ovsiannikov, and Lev Pavlovič Rapoport. "Atoms in a laser field". In: *Physics Reports* 141.6 (1986), pp. 320–433.

[105] Charles S Adams et al. "Evaporative cooling in a crossed dipole trap". In: *Physical review letters* 74.18 (1995), p. 3577.

[106] Zhao-Yuan Ma, Christopher J Foot, and Simon L Cornish. "Optimized evaporative cooling using a dimple potential: an efficient route to Bose–Einstein condensation". In: *Journal of Physics B: Atomic, Molecular and Optical Physics* 37.15 (2004), p. 3187.

[107] Lev Pitaevskii and Sandro Stringari. *Bose-Einstein condensation and superfluidity*. Vol. 164. Oxford University Press, 2016.

[108] University of Alberta Ultracold Quantum Gases Laboratory. *Evaporative cooling*. URL: `https://sites.ualberta.ca/~ljleblan/background/evaporative-cooling.html` (visited on 08/25/2021).

[109] Manuele Landini et al. "Direct evaporative cooling of 39 K atoms to Bose-Einstein condensation". In: *Physical Review A* 86.3 (2012), p. 033421.

[110] Huang Wu and Christopher J Foot. "Direct simulation of evaporative cooling". In: *Journal of Physics B: Atomic, Molecular and Optical Physics* 29.8 (1996), p. L321.

[111] ZY Ma et al. "The evaporative cooling of a gas of caesium atoms in the hydrodynamic regime". In: *Journal of Physics B: Atomic, Molecular and Optical Physics* 36.16 (2003), p. 3533.

[112] Graeme A Bird. "Molecular gas dynamics and the direct simulation of gas flows". In: *Molecular gas dynamics and the direct simulation of gas flows* (1994).

[113] OJ Luiten, MW Reynolds, and JTM Walraven. "Kinetic theory of the evaporative cooling of a trapped gas". In: *Physical Review A* 53.1 (1996), p. 381.

[114] Kirstine Berg-Sørensen. "Kinetics for evaporative cooling of a trapped gas". In: *Physical Review A* 55.2 (1997), p. 1281.

[115] Simon Baier. *An optical dipole trap for Erbium with tunable geometry*. na, 2012.

[116] T Maier et al. "Emergence of chaotic scattering in ultracold Er and Dy". In: *Physical Review X* 5.4 (2015), p. 041029.

[117] Jacob L Roberts et al. "Magnetic field dependence of ultracold inelastic collisions near a Feshbach resonance". In: *Physical Review Letters* 85.4 (2000), p. 728.

[118] PWH Pinkse et al. "One-dimensional evaporative cooling of magnetically trapped atomic hydrogen". In: *Physical Review A* 57.6 (1998), p. 4747.

[119] Matthew J Williams and Chad Fertig. "Multipartite model of evaporative cooling in optical dipole traps". In: *Physical Review A* 91.2 (2015), p. 023432.

[120] D Comparat et al. "Optimized production of large Bose-Einstein condensates". In: *Physical Review A* 73.4 (2006), p. 043410.

[121] Makoto Yamashita, Masato Koashi, and Nobuyuki Imoto. "Quantum kinetic theory for evaporative cooling of trapped atoms: Growth of Bose-Einstein condensate". In: *Physical Review A* 59.3 (1999), p. 2243.

[122] S Dzhumanov, AA Baratov, and S Abboudy. "Pairing theory of polarons in real and momentum space". In: *Physical Review B* 54.18 (1996), p. 13121.

[123] G Bismut et al. "Anisotropic excitation spectrum of a dipolar quantum bose gas". In: *Physical review letters* 109.15 (2012), p. 155302.

[124] Alex W Chin, Susana F Huelga, and Martin B Plenio. "Quantum metrology in non-Markovian environments". In: *Physical review letters* 109.23 (2012), p. 233601.

[125] Ruggero Vasile et al. "Continuous-variable quantum key distribution in non-Markovian channels". In: *Physical Review A* 83.4 (2011), p. 042321.

[126] HZ Shen et al. "Controllable dissipation of a qubit coupled to an engineering reservoir". In: *Physical Review A* 98.6 (2018), p. 062106.

[127] Magnus G Skou et al. "Non-equilibrium dynamics of quantum impurities". In: *arXiv e-prints* (2020), arXiv–2005.

[128] Arduino. *Wiring LCD to Arduino controller*. URL: `https://www.arduino.cc/en/Tutorial/LibraryExamples/HelloWorld` (visited on 08/25/2021).